NASA

Technical Memorandum TM-86090

THE CORRECTION OF ABERRATIONS COMPUTED IN THE APERTURE PLANE OF MULTIFREQUENCY MICROWAVE RADIOMETER ANTENNAS

R. F. Schmidt

May 1984

National Aeronautics and
Space Administration

Goddard Space Flight Center
Greenbelt, Maryland 20771

TM-86090

THE CORRECTION OF ABERRATIONS COMPUTED IN THE APERTURE PLANE OF MULTIFREQUENCY MICROWAVE RADIOMETER ANTENNAS

R. F. Schmidt

May 1984

GODDARD SPACE FLIGHT CENTER
Greenbelt, Maryland

All measurement values are expressed in the International System of Units (SI) in accordance with NASA Policy Directive 2220.4, paragraph 4.

THE CORRECTION OF ABERRATIONS COMPUTED IN THE APERTURE PLANE OF MULTIFREQUENCY MICROWAVE RADIOMETER ANTENNAS

R. F. Schmidt
NASA/Goddard Space Flight Center
Greenbelt, Maryland 20771

ABSTRACT

This document develops an analytical/numerical approach to identifying and correcting the aberrations introduced by a general displacement of the feed from the focal point of a single offset-paraboloid antenna used in deployable radiometer systems. A 15-meter reflector with 18-meter focal length is assumed for the analysis, which considers far-field radiation pattern quality, focal-region fields, and aberrations appearing in the aperture plane. The latter are obtained by ray-tracing in the transmit mode and are expressed in terms of optical notation. Attention is given to the physical restraints imposed on corrective elements by real microwave systems and to the intermediate near-field aspects of the problem in three dimensions. The subject of wavefronts and caustics in the receive mode is introduced for comparative purposes. Several specific examples are given for aberration reduction at eight beamwidths of scan at a frequency of 1.414 GHz.

Page intentionally left blank

Page intentionally left blank

CONTENTS

Page intentionally left blank

Page intentionally left blank

NOTATION

$\bar{n}$	unit normal to a surface
$\bar{S}_i$	incident ray vector (in context)
$\bar{S}_r$	reflected ray vector
I_1, I_2, I_3	optical invariants
h, ρ, ϕ	transverse image displacement parameter, radial and azimuthal variables
δ	phase perturbation (in context of aberrations)
W	phase coefficient (in context)
l, m, n	aberration indices
X, Y, Z	Cartesian coordinates of fundamental reference frame
θs	beam squint angle
K	beam deviation factor (in context)
D	aperture diameter
INV, EV	involute, evolute of differential geometry
Λ	wavefront
ω	*caustic (surface, line, or point in context)*
R_{AD}	radius of Airy disc
Δ	feed displacement in focal plane
(σ, ζ)	radial and azimuthal variables of offset paraboloid
F	focus or focal length (in context)
(N, ϵ)	parameters of elliptical beam
$\bar{\rho}_e$	a displacement vector
(α, β, γ)	Euler angles
Θ, Φ	polar and azimuthal angles for elliptical-beam feed
dB	decibel
$(1_x, 1_y, 1_z)$	unit Cartesian basis vectors
γ	generic symbol for surface
λ	wavelength
$\bar{K}$	vector sheet current of physical-optics theory
$\bar{H}_i$	incident magnetic field
P(I), P(J), P(K)	polarization moments
S_i	scalar weighting factor of elliptical beam (in context)
ψ_i	phase argument
Q_1	quaternion rotation operator
$Q_2, \bar{W}_2$	degenerate quaternion (vector $\bar{W}_2$)
θ_Q	rotation angle in Euclidian space (E_3)

NOTATION (Continued)

$(1, i, j, k)$	Hamiltonian basis of real quaternions
$(\alpha_Q, \beta_Q, \gamma_Q)$	direction cosines for the quaternion rotation axis
(g, h)	axial and transverse feed displacements
$\mathfrak{F}$	feed function or Fourier transform (in context)
AP	aperture
$(\bar{g}, \bar{h})$	column vectors
Γ_i	transmission coefficients
T_{ij}	transfer matrices

THE CORRECTION OF ABERRATIONS COMPUTED IN THE APERTURE PLANE OF MULTIFREQUENCY MICROWAVE RADIOMETER ANTENNAS

INTRODUCTION

The relative success of an attempt to compensate for the undesirable effects introduced by the displacement of an antenna feed from the focal point of the reflector may be evaluated by calculating (or measuring) the far-field radiation pattern. Because this pattern is the Fourier transform of an aperture distribution, an analysis of the amplitude and phase in the aperture plane for a specified polarization may reveal most of the features of the far-field pattern by inspection. An aperture plane analysis is economical since integration is not required, it provides a large amount of information, and it leads to an early diagnosis of the aberration problem.

In the present document, the transmit point of view is taken, and phase departures from an aperture plane of a paraboloidal reflector are determined and classified by analogy to an optical approach. The latter approach takes the receive point of view at a Gaussian focus and regards phase departures from a Gaussian sphere. The receive point of view is retained in the present document to locate displaced focal regions and determine their size. This is accomplished by several means, including a simple three-ray trace method, a multiray caustic analysis, and a focal region mapping based on physical optics theory. It is shown that the caustic may, alternatively, be obtained as the evolute of the received wavefront. Subsequently, the placement and size of corrective feed elements is predicated on this knowledge of the focal region.

ABERRATIONS

The aberrations observed in the focal plane of an offset paraboloid in vacuo may be due to the wavefront associated with the feed, the position of that feed with respect to the focal point of the reflector, or imperfections in the reflector itself (Ref. 1, p. 186). Assuming that the feed wavefront is spherical and the reflector is an ideal paraboloid, the feed displacement alone is responsible for the aberration. In any event, a ray trace that obeys Snell's law of reflection and accounts for optical path length yields a phase distribution in the aperture plane.

The equations,

$$\bar{n} \times \bar{S}_i = \bar{n} \times \bar{S}_r \tag{1}$$

and

$$\bar{n} \cdot \bar{S}_i = -\bar{n} \cdot \bar{S}_r \tag{2}$$

are fully descriptive regarding the angular relationship between the incident rays, reflected rays, and

surface normal, but the equation,

$$\bar{S}_r = \bar{S}_i - 2\bar{n}(\bar{S}_i \cdot \bar{n}) \tag{3}$$

is probably more useful. (See Ref. 2, pp. 354-355.)

A convenient notation for classifying aberrations in paraxial optics is one that employs the optical invariants of a symmetrical optical system,

$$I_1 = h^2, \quad I_2 = \rho^2, \quad I_3 = h\rho\cos\phi \tag{4}$$

and the expansion for the optical path difference

$$\text{OPD} = \sigma = \sum_{l,m,n} W_{2l+n,2m+n,n} h^{2l+n} \rho^{2m+n} \cos^n \phi \tag{5}$$

Here, h relates to lateral image displacement and ρ and ϕ are radial and azimuthal variables in the aperture. See Reference 3, pages 46 and 47, Reference 4, and Reference 5, page 859 for details of the classification. Large aberrations lead to all orders in the expansion. Apodization and aperture blockage have also been treated (Ref. 3, p. 95).

If certain constant terms, a_0, $b_0 h^2$, $c_0 h^4$, and $d_0 h^6$, are admitted as "aberrations," the classical aberrations of Gauss, Seidel, and Schwarzschild may be generated by simple factors, powers of the optical invariants. The aberrations of degree zero, two, four, and six emerge as products of these invariants with mixed degree of zero, one, two, and three. (See Appendix A of this document.)

An Infra-Red Handbook (Ref. 4) defines $W_{2l+n,0,0}$ equal to zero. This is explained as follows in Reference 6, pages 87 and 88. "It is customary in Hamiltonian theory to postulate that in the wavefront expansion the reference sphere for each field angle has its centre at the Gaussian image point." Also, "The constant term is omitted because in the definition of wavefront aberration we have assumed that both the wavefront and the reference sphere are chosen to pass through the centre of the pupil." In the present aperture plane analysis, the Gauss "aberrations" are retained. This was also done in Reference 5, page 858, and Reference 7, page 18, where three, six, and ten aberration terms are associated with Gauss, Seidel, and Schwarzschild, respectively.

The two views regarding the optical path difference (OPD) are illustrated in Figure 1 for an optical system and an offset paraboloid microwave reflector. It is noted that the offset reflector is inherently an asymmetrical geometry, but is a part of a parent paraboloid that is a symmetrical configuration. The development reverts to the latter, on occasion, and then proceeds after invoking a truncation argument.

The primary aberrations of Seidel are illustrated in Reference 8, page 212, as surfaces lying above or below a circular disk representative of the aperture plane. (They are not reproduced here.) It is

noted that the Cartesian aperture coordinates are

$$x = \rho \cos \phi, \; y = \rho \sin \phi \tag{6}$$

so that aberrations such as the coma term may be rewritten to advantage as

$$S_4 = W_{131} I_2 I_3 = W_{131}\, h\, \rho^3 \cos \phi = W_{131} h\, (x^3 + xy^2) \tag{7}$$

to exhibit cross-gradients among the phase variations.

CAUSTIC SURFACES AND WAVEFRONTS

The receive point of view may be taken to obtain an appreciation of the behavior of the offset paraboloid for various angles of wave arrival, initially in the limit of zero wavelength, by means of caustic surface analysis. Detailed discussions of point, line, and surface caustics are found in Reference 8, page 792; Reference 9, page 498; and Reference 10, page 526. "One of the earliest discoveries in optics (F. Maurolycus, 1575) was that the rays of a normal system are tangential to a surface, the so-called caustic surface, and that the general ray is tangential to the caustic in two points." (See Ref. 9, p. 156.) The caustic has physical reality (Ref. 11, p. 79). It may be defined as the envelope to a system of rays of an orthotomic system or the locus of the principal centers of curvature of a wavefront (Ref. 12). Used in conjunction with a "spot diagram," the intersection of rays with a chosen image plane, the caustic surface approach leads to useful impressions of geometrical image quality and intensity (Ref. 6, p. 93).

The offset paraboloid geometry of the present discussion is shown as Figure 2, together with the surface-generating equations and assumed parameters. A system of three rays at plane-wave incidence 0° and -8° is shown in Figure 3. From this figure, it may be inferred that the focal axis and focal plane of an offset paraboloid are not the same as for the parent paraboloid, although the geometrical focal point is the same. Furthermore, the central ray of the three-ray approach is seen to be strongly indicative of the approximate focal axis (AFA) for various angles of wave arrival. The approximate focal plane (AFP) was, by analogy to parent paraboloids, initially taken to be orthogonal to AFA and passed through the focal point (F). The AFP was not obvious for general angles of arrival since the displaced pseudofocus (F′) is not known prior to a focal region mapping.

A ray trace based on 15 rays (Figure 4) maps an arc of the caustic surface in the x-z plane for a plane-wave angle of arrival of (-8°). An approximation formula relating the angle of arrival (θ_s) to the lateral feed displacement (Δ) of a parent system of focal length (F) is:

$$\sin \theta_s = \frac{K\Delta}{F} \tag{8}$$

Here, K is a beam-deviation factor (Ref. 1, p. 488). Further,

$$0.92 \leq K \leq 1.00 \tag{9}$$

for

$$0.50 \leq F/D \leq 1.00 \tag{10}$$

of the parent system. If the approximation formula is applied to the offset geometry, and Δ is now taken to lie in the inclined focal plane AFP(0°) as shown, the location of the pseudofocus (F′) may be estimated. It is seen to fall on the caustic arc for $\theta_i = -8°$, but is not in the center of that arc. Rather, it is situated near one end of the caustic arc (K ≈ 1.0 assumed, $F/D_p = 0.5$, $F/D_o = 1.2$).

Returning to the parent paraboloid, it is instructive to further develop the caustic, here based on 16 rays, and identify the bounding rays (1, 7, and 16) for the offset and parent surfaces as seen in the x-z plane of Figure 5. The caustic arc is nearly circular for the truncation of the parent paraboloid shown. This fact may be exploited to develop the involute (INV) of the caustic (ω), or reflected wavefront (Λ), since parameterizations by arc length are sometimes difficult to formulate. The caustic (ω) is the evolute (EV) of wavefront (Λ). These concepts will be developed subsequently for the offset paraboloid geometry.

For the present it is merely noted that:

$$EV(\Lambda) = \omega \tag{11}$$

and

$$INV(\omega) = \Lambda \tag{12}$$

It follows that:

$$INV\,[EV(\Lambda)] = \Lambda \tag{13}$$

and

$$EV\,[INV(\omega)] = \omega \tag{14}$$

where ω may have branches (ω_1 and ω_2) as mentioned previously.

The nearly circular caustic arc of Figure 5 is actually part of an inclined and translated curve known as Tschirnhausen's cubic (Ref. 2, p. 25). It has been associated with corrective lens methods for offset paraboloids. Figure 6 shows the analytical caustic curve, which is equivalent to the envelope of rays tangent to that curve. The offset surface and incident plane wave comprise an asymmetrical geometry, but Tschirnhausen's cubic is a symmetrical function given by:

$$\overline{(x'')^2} = y''\,(y'' - b)^2/3b \tag{15}$$

$$b = 9a \sin\theta \tag{16}$$

The inclination of the (x'', y'') coordinate frame equals θ, and the translation follows from

$$x' = \frac{(y')^{1/2}(y' - 9a \sin\theta)}{(27a \sin\theta)^{1/2}} + a\cos\theta, \tag{17}$$

when y' and y'' are indistinguishable, upon setting (y') equal to zero. (See References 13 and 14.) The rotation transformation is given by:

$$x = x' \cos\theta + y' \sin\theta \tag{18}$$

$$y = y' \cos\theta - x' \sin\theta \tag{19}$$

Finally, to arrive at the coordinates of Figure 6, the correspondence,

$$x \text{ of } (18) - a \rightarrow z \tag{20}$$

$$y \text{ of } (19) \rightarrow x \tag{21}$$

is made. It can be seen that the appropriate segment of arc on the Tschirnhausen cubic curve is determined by the parent or offset paraboloid truncation. For the parent and offset reflectors of Figure 6, the bounding tangents intercept the cubic curve in the essentially circular part of that curve as shown previously by the envelope of the caustic (Figure 5). The cubic is extended here to display its symmetric form, principal axis intercepts, etc.

Returning to the offset paraboloid and the microwave aberration problem, a set of caustic arcs is now developed corresponding to plane-wave angles of incidence equal to 0°, –4°, –8°, –16°, and –32°. Figure 7 shows the bounding and central tangent rays for each angle of incidence and the associated arc along each cubic curve. The shaded zone illustrates the continuous and rapid increase in the caustic arc length with increasing (absolute) angle of incidence. An aberration problem attending the larger angles of wave arrival may therefore be represented by the phase departure from an aperture plane (ray-trace program data), the equivalent expansion (equation 5), or a part of a caustic surface. For simplicity, caustic arcs were illustrated here. A detailed development of the caustic surface for the offset paraboloid will be deferred to another Technical Memorandum. An appreciation of the complexity of the undertaking, which includes phase information on the caustic surface, may be obtained from Reference 15.

FOCAL REGION MAPPING

In an attempt to determine the focus of the offset paraboloid for –8.7° plane-wave incidence several methods, including complex-vector physical optics theory, were employed. The focal-region electric field was first computed for axial plane-wave incidence to verify the inclination angles of

the focal axis and focal plane. Figure 8 shows agreement with previous ray-trace results. A comparison of the radius of the Airy disk for the offset paraboloid, surface integration sampling interval equal to 2.0 λ, is made with the approximation formula for parent paraboloids:

$$R_{AD}^{(0^\circ)} = \frac{1.22\,F\lambda}{D} = \frac{(1.22)(18.0)\lambda}{(15.0)} = 1.46\,\lambda \approx 0.31 \text{ m (theoretical)} \qquad (22)$$

$$R_{AD}^{(0^\circ)} \approx 1.75\,\lambda \approx 0.37 \text{ m (from Figure 8)} \qquad (23)$$

The physical optics formulation and the parameters used to compute the focal-region fields at 0.0° and -8.7° plane-wave incidence are given in Appendix B of this document.

Figure 9 shows the result of the -8.7° plane-wave computation, surface integration sampling interval equal to 1.0 λ, at 1.414 GHz (λ = 0.21 m). The maximum value of the electric field appears to be at (x_e, y_e, z_e) = (2.8 m, 0.0 m, -1.3 m), and the isophotes or constant-intensity contours are rather symmetrically disposed about that point out to 1 meter. Beyond 1 meter, the asymmetries of the offset reflector/incident wave system can be seen. The radius of Airy disk for -8.7° plane-wave incidence has been greatly affected:

$$R_{AD}\,(-8.7^\circ) > 7\lambda \text{ or} > 1.5 \text{ m} \qquad (24)$$

Note that the caustic arc length at -8.0° incidence is 4.0 m (Figure 7).

ESTIMATES OF THE DISPLACED FOCUS

An estimate of the position of a displaced focus of an offset paraboloid for a given plane-wave incidence angle may be obtained by various means. A comparison of results is now made for the geometry of Figure 2 for an angle of plane-wave arrival equal to -8.7°. Figure 10 illustrates that the reflector and feed position information (x_e, y_e, z_e) is obtained by several means. Figure 11 is an expanded-scale version of Figure 10.

(F_1') (x_e, y_e, z_e) = (2.56, 0.0, -1.6) m
$\Delta \approx F \sin\theta / K$; θ = 8.7°, F = 18.0 m, AFP (0°)
F/D_o = 18.0/15.0 = 1.2, F/D_p = 18.0/36.0 = 0.5
K ≈ 1.0, 0.9, 0.8 (Ref. 1, p. 488)
Comment: valid for small θ.

(F_2') (x_e, y_e, z_e) = (2.80, 0.0, -1.8) m, LI = 2.0 (λ)
Focal Region Map (Physical Optics)
Comment: Generally reliable for larger θ, but integration interval is large. Based on field symmetry.

(F_3') (x_e, y_e, z_e) = (parabolic arc information only)

$z_\ell = \frac{\sigma_\ell^2}{4\,(2F)}$; AFA (0°) inclination

Parabolic arc with vertex at origin (0).
Attributed to P. Potter
Comment: Arc has negligible departure from AFP (0°).

(F_4') (x_e, y_e, z_e) = (2.8, 0.0, -1.3) m, LI = 2.0 (λ)
(x_e, y_e, z_e) = (2.8, 0.0, -1.3) m, LI = 1.0 (λ)
Focal Region Map (Physical Optics)
Comment: Generally reliable for larger θ, two integration intervals used. Based on maximum electric field (E_{max}) value.

(F_5') (x_e, y_e, z_e) = (2.25, 0.0, -2.00) m
Intersection of two tangent rays $R_2 \cap R_3$ (Figure 10)
Comment: Experience has shown that the $R_2 \cap R_3$ approach gives good results for small θ.

(F_6') (x_e, y_e, z_e) = (circular arc information only)
R = F about vertex (V) as center (offset paraboloid)
R = OC about midpoint (C) as center (parent paraboloid)
Attributed to Silver, adaptation by author.
Comment: Valid for small θ.

(F_7') (x_e, y_e, z_e) = (1.8, 0.0, -2.5) m
Based on center of caustic arc bounded by R_1, R_3
(Figure 7, -8.7° interpolated)
Comment: Large departure from other methods.

(F_8') (x_e, y_e, z_e) = (not done)
Focal Region Map
Comment: Generally reliable for larger θ. Based on flatness of field (wavefront).

(F_9') (x_e, y_e, z_e) = (not done)
Focal Region Map
Comment: Generally very reliable for larger θ. Based on time-average Poynting vector.

ABERRATION CORRECTION (I)

On the premise that a given reflector antenna is able to concentrate the energy of an off-axis incident plane wave in a rational "focal region," it is necessary to move the primary feed to that region (Ref. 5, p. 860). Subsequently, it may be possible to adapt to the received field distribution and in some sense attain a "matching" feed that favors antenna gain, beamwidth, sidelobe levels, gain-beamwidth product, a polarization characteristic, etc. Situations arise in which the reflector should be replaced with an adaptive array. It is assumed here that the reflector still focuses satisfactorily, but that one or more aberrations should be reduced, if not altogether eliminated, by combination methods if necessary.

Aberrations that are commonly encountered include transverse focus ($W_{111}\ I_3$), axial focus ($W_{020}\ I_2$), coma ($W_{131}\ I_2\ I_3$), and spherical ($W_{040}\ I_2^2$). See Appendix A-2 for additional aberrations. Transverse focus ($W_{111}\ I_3$) is essential to beam squinting, is induced by a nonzero value of (h) representing lateral feed displacement, and is actually not an aberration affecting image quality. By the shift theorem of Fourier transform theory, it is shown that this phase gradient displaces a beam in space, but does not distort the beam. (See Ref. 16, p. 282, and subsequent discussion in this document.) The symmetrical aberrations, axial and spherical, may be dealt with by feed displacement. Nonvanishing lateral displacement (h) also introduces the asymmetrical comatic aberration ($W_{131}\ I_2\ I_3$), which manifests itself in radiation patterns as raised and lowered sidelobes in the cut of the cubic phase gradient (Ref. 5, p. 859). It constitutes a significant limitation for radiometer antennas.

In an initial attempt to minimize coma, the feed function

$$\mathcal{F} = \frac{\cos^N \Theta}{\left[\sin^2\Theta\cos^2\Phi + \frac{\sin^2\Theta\sin^2\Phi}{(1-\epsilon^2)} + \cos^2\Theta\right]^{1/2}} \tag{25}$$

was developed and used to mathematically simulate five differentially phased, linearly polarized, elliptical beams with common phase centers and 3-dB crossover levels. The angular beam separation was set at 9 degrees ($\Delta\beta$) at 1.414 GHz, spatial rotation being obtained by means of Euler angles ($\alpha = 90°, \beta, \gamma = 0°$). The third primary beam (i = 3) was directed at the center (C) of the offset paraboloidal reflector (Figures 12 and 13) as the pseudofocus (F′) moved away from the focus (F) with increased plane-wave angle of arrival (main-beam scan angle).

Since the electric field at theta (Θ) equal to 0° is unity, using equation 25,

$$dB = 20\,N \log_{10}\frac{1}{\cos\Theta} + 10 \log_{10}\left[\sin^2\Theta\cos^2\Phi + \frac{\sin^2\Theta\sin^2\Phi}{(1-\epsilon^2)} + \cos^2\Theta\right] \tag{26}$$

for all values of directivity parameters (N) and (ϵ). It may be verified that:

$$N = 22.8, \quad \epsilon = 0.995827 \tag{27}$$

for an elliptical beam with -3 dB beamwidths of 19.88° and 9.0°. After Euler-angle rotation ($\alpha \approx 90°$), the semimajor axis of the elliptical beams is parallel to vector 1y, as shown in Figure 14. The parameter N = 22.8 results in a -15.0 dB feed edge-taper in the y-sense for the central beam (i = 3) with $\beta = 31°$. The edge-taper in the x-sense was subsequently varied by controlling the excitation (S_i) for the individual beams; this is identified for the individual radiation patterns presented in this document by means of a graphic symbol for both amplitude (S_i) and phase (ψ_i) of the beams (i = 1, 2, . . ., 5).

Returning to Figure 13, it can be seen that the 9° beamwidth is associated with a corresponding feed dimension:

$$D_{\mathcal{F}} = \frac{70\lambda}{BW^{\circ}\ (-3\ dB)} \approx \frac{70\lambda}{9} \approx 8\lambda = 1.7\ m \tag{28}$$

to the nearest integer multiple of half-wavelength. Defining far field for the feed in terms of

$$R_c \approx D^2_{\mathcal{F}}/\lambda = 64\lambda = 13.5\ m \tag{29}$$

it is concluded that the five prime-feed radiation patterns are everywhere Fraunhofer patterns, as seen from the surface of the offset paraboloid (γ). It is noted that the radius of the Airy disk for -8° plane-wave incidence, obtained by physical optics theory using a one-wavelength integration sampling interval and an annular disposition of samples over the reflector (γ), is approximately 1.5 m. The inference is that the displaced Airy disk diameter ($D'_{AD} \approx 3.0$ m) is able to accommodate the feed length ($D_{\mathcal{F}} \approx 1.7$ m).

Before the coma-correction simulation described above was implemented, several reference patterns were computed. The offset paraboloid was first illuminated by a single pencil beam (i = 1), with -15 dB feed edge-taper, directed at the center of the reflector (C) (Figure 2). Feed directivity was controlled by parameters (N, ϵ) = (22.84, 0.0) and beam-pointing by Euler angles (α, β, γ) = (90.0°, 31.0°, 0.0°). The feed intensity was arbitrarily set at unity ($S_1 = 1.0$), and the initial phase at zero ($\psi_1 = 0.0^{\circ}$). A linear polarization moment (P(I) = 1.0) in the (1_x) direction was effectively converted to P(J) = 1.0 in the (1_y) direction under the assumed ($\alpha = 90.0^{\circ}$) Euler-angle rotation of the prime feed in this simulation. The feed displacement was taken to be zero ($\bar{\rho}_e = 0.0$).

A half-planar cut ($\phi = 180^{\circ}$) of the resulting far-field physical optics radiation pattern is shown in Figure 15. Beamwidth (degrees) is shown for -3.0, -10.0, and -20.0 dB relative to the beam maximum. The first sidelobe was computed at -29.3 dB, and is due to the combination of feed taper, space divergence of the prime-feed fields, and the law of current induction on the surface of the offset paraboloid:

$$\bar{K} = 2\bar{n} \times \bar{H}_1 \tag{30}$$

This secondary beam is not squinted ($\theta_s = 0^{\circ}$) and exhibits no aberrations since the feed phase center was taken to be at the focus (F) of the offset reflector under $\bar{\rho}_e = 0.0$.

In order to verify the simulation when using five (i = 5) elliptical prime-feed beams, a simple configuration was selected. The individual beam intensities were set to unity ($S_i = 1.0$) and the initial phases to zero ($\psi_i = 0.0^{\circ}$). Beam ellipticity was obtained as indicated by equation 27, (N, ϵ) = (22.84, 0.995827). The central beam (i = 3) was directed at point C from the focus (F) by setting ($\bar{\rho}_e = 0.0$) and Euler angles ($\alpha_3, \beta_3, \gamma_3$) = (90.0°, 31.0°, 0.0°). Effective polarization was again P(J) = 1.0. The incremental angle ($\Delta\beta$) was set at a constant value (9.0°).

A half-planar cut ($\phi = 180°$) of the resulting far-field physical optics radiation pattern is shown in Figure 16. Beamwidths are given at three power levels as before. Note that the half-power beamwidth is slightly smaller than in Figure 15, which is to be expected since the individual beam intensities were equal. The first sidelobe level was -18.0 dB. This result agrees with the fact that uniform illumination for a circular aperture is associated with a -17.6 dB first sidelobe level. The value $e = 0.995827$ has introduced a slight taper in the vicinity of the reflector edges ($\beta = 9°, 53°$). It was concluded that this mathematical simulation for five beams was correct and could be used to explore coma correction techniques.

The prime feeds used to compute the radiation patterns of Figures 15 and 16 were next translated to a point in the approximate focal plane of the offset paraboloid: $\overline{\rho}_e = (1.2720, 0.0, -0.7949)$ meters. The angle β was updated from 31.0° to 34.0° so that the single pencil beam under (i = 1) and the central beam under (i = 5) would again be directed to point (c) on the paraboloid. Figures 17 and 18 show the far-field or Fraunhofer radiation patterns, and beamwidths are identified as before. The coma lobes for these simulations are at -20.0 and -12.8 dB, $\theta_s = 4.3°$, and should be compared to -29.3 and -18.0 dB, $\theta_s = 0.0°$.

Prior to attempting coma correction, by introducing discrete phase differentials among the five elliptical beams, a conservative discrete amplitude taper was selected for these prime-feed beams: $S_1 = S_5 = 0.316$, $S_3 = 1.0$, $S_2 = S_4 = 0.562$. This program input had the effect of producing a progressive taper of -5 and -10 dB to either side of the central beam. The result is given by the radiation pattern of Figure 19, which shows a -19.0 dB coma lobe.

The objective of reducing coma by compensating the cubic phase gradient with five primary beams having a common phase center ($\overline{\rho}\epsilon_i$ = constant, i = 1, 2, . . ., 5) was approached by attempting to optimize the phase of the beams corresponding to i = 3, 4, 5 while holding the amplitude taper $S_1 = S_5$, $S_3 = 1$, $S_2 = S_4$ indicated above. In addition, phase variations that were arbitrary and departed from the theory were explored to further verify program behavior. A few of the results are presented here.

The phase parameter (ψ_5) was varied over wide latitudes for the selected amplitude taper among the five beams, and it was concluded that a value ($\psi_5 = -135.0°$) was very close to optimum. An angular increment of $\Delta\beta = 9.0°$ was retained, and the central beam angle of $\beta_3 = 36°$ was eventually used. Coma reduction was found to be rather insensitive to the set of angles (β_i) since the latter affect illumination intensity, spillover, etc. for beams with a common phase center. A coma lobe of -22 dB level was obtained by varying (ψ_5) alone. (See Figure 20.)

Similarly, the phases of (ψ_5) and (ψ_4) were varied simultaneously, in accordance with and contrary to a cubic law across the aperture in a vertical (1_x) sense. It was concluded that values $\psi_5 = -130.0°$, $\psi_4 = -30.0°$ were close to optimum for coma-lobe reduction. A coma lobe of -28.3 dB level was obtained by varying ψ_5 and ψ_4 simultaneously. (See Figure 21.) It is noted that this beam exhibits approximately -30 dB first minima and sidelobe levels and beamwidth similar to those obtained in Figure 15, an unscanned case obtained with symmetric -15.0 dB feed taper.

The phases of (ψ_5, ψ_4, ψ_3) were varied simultaneously, and although some beam characteristics changed, no significant improvement over the result given as Figure 21 was obtained. At this stage of the exploration, a decision was made to calculate the orthogonal radiation pattern cut. Since the beam of Figure 21 is squinted ($\theta_s = 4.5°$) an *in-situ* orthogonal cut through the beam maximum would imply both θ and ϕ variation with attendant plotting difficulties. Alternatively, a proper rotation of the entire discrete current distribution of the physical optics calculation by $\theta_s = 4.5°$ would place the beam maximum on the ($+1_z$) axis again. Consequently, any radiation pattern cut through the beam maximum can be made by setting ϕ = constant and treating θ as the single independent variable.

The rotation of sheet current values ($\bar{K}$) to obtain a new set ($\bar{K}'$), as described above, was made simply by means of a quaternion transformation. A set of position vectors ($\bar{\rho}$) of ($\bar{K}$) on the offset paraboloid was converted into a new set ($\bar{\rho}'$) of ($\bar{K}'$) by the identical transformation. These operations made possible the integration of sheet current, weighted by incremental reflector area, under the physical optics algorithm with minimal reprogramming effort. Vectors ($\bar{K}$) and ($\bar{\rho}$), above, may be regarded as "free" and "bound" vectors, respectively, in the present context. The same holds true for their counterparts ($\bar{K}'$) and ($\bar{\rho}'$).

A protracted discussion of quaternions is inappropriate here. It may be worth noting that a rotation in the amount θ_Q in physical 3-space (E_3) appears as a half-angle or $\theta_Q/2$ operator in a transformation that resembles the similarity transformation of classical physics. The general rotation is executed about a preferred axis whose direction cosines are (α_Q, β_Q, γ_Q), not to be confused with Euler angles (α, β, γ) used previously. In conclusion, the quaternion (Q_2) simplifies to a vector ($\bar{W}_2$) of E_3, and

$$\bar{W}_2' = Q_1 Q_2 Q_1^{-1} = Q_1 \bar{W}_2 Q_1^{-1} \tag{31}$$

take

$$Q_1 = \cos\frac{\theta_Q}{2} + (i\alpha_Q + j\beta_Q + k\gamma_Q)\sin\frac{\theta_Q}{2} \tag{32a}$$

and

$$Q_1^{-1} = \cos\frac{\theta_Q}{2} - (i\alpha_Q + j\beta_Q + k\gamma_Q)\sin\frac{\theta_Q}{2} \tag{32b}$$

See References 17, 18, and 19 for background material. Note that (ij) equals (k), (k^2) equals (–1), (kj) equals (–i), etc.

The orthogonal pattern cut required here is made by setting $\theta_Q = \theta_s$, $\alpha_Q = 0$, $\beta_Q = 1.0$, $\gamma_Q = 0.0$, $\phi = 90°, 270°$. Here, θ is the independent variable as with unscanned beams.

Using the same program parameters as those for Figure 21, the $\theta = 90°, 270°$ cut effectively coalesces the aperture distribution to a line parallel to the (1_y) axis. A radiation pattern whose –10

and -20 dB beamwidths are somewhat too broad was obtained by physical optics and is given as Figure 22. It shows a vestigial sidelobe of -22.0 dB level, about 6 dB worse than the corrected coma-lobe level and 3 dB better than the uncorrected coma-lobe level (Figures 19 and 20, respectively). The necessity of verifying final radiation patterns by means of principal plane and diagonal plane cuts, at least, is apparent.

ABERRATION CORRECTION (II)

Attempts to minimize coma for increased plane-wave angle of arrival ($\theta \approx -8°$) at a frequency of 1.414 GHz for the assumed geometry proved difficult. Since the effective aperture was diminished significantly, beamwidths increased. Estimation of $\overline{\rho}_e$ for feed positioning by various means was tedious. (See Figures 10 and 11.) Previously, F′ was taken to lie in the aperture plane ($\theta \approx 4°$) and $\overline{\rho}_e$ was determined accordingly. This approach was now unsuccessful. A review of the assumptions and an alternate approach were sought. The issue of apodization (taper) was set aside, and the phase aberration analysis was reviewed.

The large wave-angle ($\theta \approx -8°$) indicated a radical departure from Gaussian optics, and the assumption of an offset paraboloid violated Hamilton's condition that the instrument be symmetrical. It was noted that the aberration expansion of equation 5 provided for lateral feed displacement (h) relative to the system or focal axis (z), but exhibited no comparable axial feed displacement term (g). Also, the focal axis of the parent paraboloid and offset paraboloids did not coincide. Could (h′) be assumed a lateral displacement with respect to z′, the approximate focal axis of the offset paraboloid? Further, if the expansion 5 contained only particular orders of terms, was it capable of representing the phase aberrations in the aperture plane of the offset paraboloid for large wave angles ($\theta \approx -8°$)?

A ray-optics program was used to obtain the aberrations in the aperture plane of the antenna. The line cut (y = 0) in the ±x direction was selected from the aberration surface, corresponding to ϕ = 0°, 180°, and a restricted expansion in powers of aperture radius (ρ) was made. It was tacitly assumed that terms up to and including the fourth power of ρ might suffice. Good closure verified this assumption. In effect, the classical aberrations were rewritten:

$$W_{111}\, h\rho \cos\phi \rightarrow (W_{111} h)\,\rho \tag{33}$$

$$W_{020}\,\rho^2 \rightarrow (W_{020})\,\rho^2 \tag{34}$$

$$W_{131}\, h\rho^3 \cos\phi \rightarrow (W_{131} h)\,\rho^3 \tag{35}$$

$$W_{040}\,\rho^4 \rightarrow (W_{040})\,\rho^4 \tag{36}$$

Preservation of the original concept of (h) orthogonal to z, or (h′) orthogonal to z′ in the present case, was no longer required. The objective was simply to map coefficients, such as the associated terms (W_{131} h), in the focal region. This was done for both a parent and an offset paraboloid,

$$F/D_p = 18\ m/36\ m = 0.5 \tag{37}$$

$$F/D_o = 18\ m/15\ m = 1.2 \quad , \tag{38}$$

by selecting values of $\bar{\rho}_e$ on a Cartesian grid in the (xz) plane.

Figures 23 through 26 illustrate the coefficients associated with lateral focus, axial focus, coma, and spherical aberration of a symmetric parent paraboloid. It can be seen from Figure 23 that the classical aberration for lateral focus is observed along the system axis (z) for which (h) equals zero. For small nonzero values of (h), the lines

$$G_2 = (W_{111}\ h)\,\rho = \text{constant} \tag{39}$$

are nearly parallel to z. As the departure from Gaussian optics increases, (G_2) is seen to be constant along curved lines. Because the ($\cos\phi$) term has been suppressed, the coefficients assume positive or negative values.

The axial focus coefficients are independent of lateral image displacement in the classical discussions where axial image displacement (g) is not introduced. In the xz plane,

$$|\bar{\rho}_e| = (g^2 + h^2)^{1/2} \quad . \tag{40}$$

The lines

$$G_1 = (W_{020})\,\rho^2 = \text{constant} \tag{41}$$

are shown in Figure 24. They assume positive or negative values also and are essentially circular arcs.

The coma coefficients are displayed in Figure 25. It can be seen that the classical aberration is observed along the system axis (z) for which (h) equals zero, as was the case for lateral focus. For small nonzero values of (h), the lines

$$S_4 = (W_{131}\ h)\,\rho^3 = \text{constant} \tag{42}$$

are nearly parallel to z, but become curves as the assumption of Gaussian optics is increasingly violated.

Finally, Figure 26 displays the spherical coefficients, also independent of (h) in the classical or receive sense. The lines for which

$$S_1 = (W_{040})\,\rho^4 = \text{constant} \tag{43}$$

appear to be parabolic arcs with positive or negative values. It may be verified that the contribution of this aberration term, on an absolute basis,

$$0 \leq \rho \leq 1 \tag{44}$$

is rather negligible in the present discussion.

Figures 27 through 30 illustrate the same coefficients as Figures 23 through 26, but apply to the offset paraboloid. Figure 27 suggests that the inclined focal axis (z′) may replace z, and (h′) may be taken orthogonal to z′ in analogy with parent paraboloids, and this is also borne out by computed radiation pattern squint angles. Figure 28 shows essentially circular arcs and should be compared to Figure 24, but the center of those arcs is not along z′. Figure 29 shows curved lines somewhat similar to those in Figure 25, but symmetry about z′ is lacking. Figure 30 departs drastically from the parabolic arcs of Figure 26, although some vestiges remain. Symmetry about z′ is lacking.

In conclusion, it is difficult to obtain a close analogy between the parent and offset paraboloid behavior. The asymmetric offset paraboloid has distinct features. Introduction of (h′) and z′ sets the lateral focus analysis on a one-to-one basis between the parent and offset paraboloids. The advantage gained by mapping the modified aberration coefficients of Figures 27 through 30 is that a strategy for selecting ($\bar{\rho}_e$) can be developed and trade-offs between various aberration terms can be determined quantitatively. It is noted that the present approach was restricted to the line (±x, y = 0) in the aperture plane. The implication is that the aberration coefficients should, properly, be mapped for other lines (y ≠ 0) in the aperture plane.

An immediate simplification, predicted in Figure 27, is that the beam angle (θ_s) can be held constant while coma-lobe reduction is being carried out. It can also be seen that minimization of the term associated with coma, by intersecting the arc

$$(W_{131}\, h) = 0 \tag{45}$$

along a line

$$(W_{111}\, h) = \text{constant} \tag{46}$$

Figure 29 results in an enormous increase in the axial aberration. The departure from the arc

$$(W_{020}) = 0 \tag{47}$$

of Figure 28 is excessive. It may be instructive to locate the phase center of a multibeam array situated at

$$\bar{\rho}_e = (1.68, 0.0, -2.0)\ \text{meters} \tag{48}$$

in Figures 27 through 30 and compute the aberration values introduced. Once $(\overline{\rho}_e)$ has been selected, the task of determining the relative phases (ψ_i), between these beams with common phase center, may be undertaken to reduce coma.

Figure 31 shows the result after optimizing the set of phase values (ψ_i) for the feed position $(\overline{\rho}_e)$ of equation 48. A coma lobe of −26 dB was obtained, 1 dB lower than the first local maximum at $\theta = 9.8°$ on the opposite side of the main beam. Beamwidths are given at four power levels.

FOURIER TRANSFORMS

As the present study of the correction of aberrations computed in the aperture plane of the offset paraboloid antenna progressed, the Fourier transform became ubiquitous. In anticipation of a more fully automated computer program in which the criteria of aberration correction are established in the aperture plane, rather than in the far-field region, the role of the Fourier transform becomes increasingly important. Although two-dimensional transforms are required throughout, and even three-dimensional transforms could be used to advantage when dealing with the paraboloid, the subsequent discussion is restricted to one-dimension for convenience.

Beginning with the relationship between the paraboloid antenna aperture distribution (AP_γ) and the far-field radiation pattern E (θ, ϕ), the definition of the Fourier transform and its inverse are applicable as indicated previously (Ref. 16, p. 275 and Ref. 20, pp. 11 and 13):

$$H(f) = \int_{-\infty}^{\infty} h(t)\, e^{-j2\pi ft}\, dt \tag{49}$$

and

$$h(t) = \int_{-\infty}^{\infty} H(f)\, e^{j2\pi ft}\, df \tag{50}$$

Alternatively,

$$\mathcal{F}\,[h(t)] = H(f) \tag{51}$$

and

$$\mathcal{F}^{-1}\,[H(f)] = h(t) \tag{52}$$

Next, as a direct consequence of these definitions, the Fourier transform isolates the Gaussian aberration,

$$G_2 = W_{111}\, I_3 \tag{53}$$

from other aberrations that affect image quality. Since the introduction of a linear phase gradient ($e^{j2\pi fot}$) results in

$$\mathcal{F}(AP_\gamma) = \mathcal{F}\,[h(t)\,e^{j2\pi fot}] = \int_{-\infty}^{\infty} f(t)\,e^{-j2\pi(f-fo)t}\,dt = H(f-fo) \quad , \qquad (54)$$

the shift theorem that ensures distortionless beam-swinging is established (Ref. 16, p. 282, and Ref. 21, p. 84). Equation 54 is sometimes referred to as the frequency-shifting property of the Fourier transform.

Following this, the concept of a transform of a transform appears in several contexts. Given a prime-feed distribution ($AP_{\mathcal{F}}$) at focus (F) whose spatial Fourier transform leads to the paraboloidal antenna aperture distribution ($AP_{\mathcal{F}}$), to within a space divergence factor (r^{-1}) and a minor perturbation due to the law of current induction (equation 30), it follows that:

$$\mathcal{F}[\mathcal{F}(AP_{\mathcal{F}})] = \mathcal{F}\,(AP_\gamma) = E\,(\theta,\phi) \quad . \qquad (55)$$

Consecutive transforms may also occur with circuits and will be discussed in greater detail in connection with the Butler beam-forming matrix (Ref. 22 and Ref. 23, p. 258). Since the circuits may lead to the prime-feed distribution, cascaded transforms arise. A specialization of the concept is sometimes referred to as the symmetry property of the Fourier transform and follows from re-writing equation 50 as:

$$h(-t) = \int_{-\infty}^{\infty} H(f)\,e^{-j2\pi ft}\,df \qquad (56)$$

and interchanging parameters t and f, so that

$$\int_{-\infty}^{\infty} H(t)\,e^{-j2\pi ft}\,dt = h(-f) \quad . \qquad (57)$$

There is no truncation of H(t) in equation 57, which differs from equation 55. The concept of a transform of a transform is therefore also useful for extending Fourier transform tables without calculating new transforms (Ref. 21, p. 85, Ref. 20, p. 32, and Ref. 24, p. 196).

Of particular interest in the reduction of aperture aberrations are the Fourier transforms of uniform continuous and discrete distributions. The former is an idealization of the latter regarding prime feeds, but may also be used to generate a reference for paraboloids:

$$H(f) = \int_{-T_o}^{T_o} A\,e^{-j2\pi ft}\,dt = 2AT_o\,\frac{\sin(2\pi T_o f)}{(2\pi T_o f)} \quad . \qquad (58)$$

Here, aperture width equals $2T_o$, and A equals a real constant (Ref. 20, p. 24, and Ref. 21, p. 78). The above, particularly relevant for the prime-feed array associated with the Butler matrix, is modified by the shift theorem, and

$$\mathcal{F}[\delta(t-t_o)] = \int_{-\infty}^{\infty} \delta(t-t_o) e^{-j2\pi ft} dt = e^{-j2\pi ft}\Big|_{t=t_o} = e^{-j2\pi ft_o} \quad , \tag{59}$$

Reference 21, page 10, together with the linearity (superposition) property of Fourier transforms (Ref. 21, p. 82):

$$\mathcal{F}[a_1 h_1(t) + a_2 h_2(t)] = a_1 H_1(f) + a_2 H_2(f) \quad . \tag{60}$$

Here

$$\mathcal{F}[h_1(t)] = H_1(f) \tag{61}$$

and

$$\mathcal{F}[h_2(t)] = H_2(f) \quad . \tag{62}$$

In the case of a uniform array of (n_s) discrete sources a distance (t_o) apart, with one source on the coordinate origin,

$$\mathcal{F}\left\{\sum_{1}^{ns} A\,\delta[t-(n_s-1)\,t_o]\right\} = H(f) = \sum_{1}^{ns} A\, e^{-j2\pi f(n_s-1)t_o} \quad . \tag{63}$$

Then

$$H(f) = A\left(1 + e^{-j2\pi f(t_o)} + e^{-j2\pi f(2t_o)} + \ldots + e^{-j2\pi f(n_s-1)t_o}\right) \tag{64}$$

and

$$H(f)\, e^{-j2\pi f t_o} = A\left(e^{-j2\pi f(t_o)} + e^{-j2\pi f(2t_o)} + \ldots + e^{-j2\pi f(n_s)t_o}\right) \quad , \tag{65}$$

so that

$$H(f) - H(f)\, e^{-j2\pi ft_o} = A\left(1 - e^{-j2\pi f n_s t_o}\right) \quad . \tag{66}$$

From this result,

$$H(f) = A \frac{\left(1 - e^{-j2\pi f\, n_s t_o}\right)}{1 - e^{-j2\pi f\, t_o}} = A \frac{\sin\left[(2\pi f\, t_o)\, n_s/2\right]}{\sin\left[(2\pi f\, t_o)/2\right]} e^{-j(2\pi f\, t_o)(n_s - 1)/2} \tag{67}$$

prior to the application of the shift theorem, which introduces a linear phase gradient. This result for the linear array of discrete sources should be compared to equation 58, a continuous linear distribution. If, in a physical application, each element width of the uniform array equals t_o,

$$(2\, T_o) = (n_s\, t_o) = \text{feed width} \quad . \tag{68}$$

Equation 6 may be generalized (Ref. 25, p. 451) for a cubic lattice array that is directly applicable in mathematical simulations of Butler array matrix feeds.

Following Reference 25, let

$$\gamma_1 = ka_1 \sin\theta \cos\phi + \alpha_1 \tag{69}$$

$$\gamma_2 = ka_2 \sin\theta \sin\phi + \alpha_2 \tag{70}$$

$$\gamma_3 = ka_3 \cos\theta + \alpha_3 \quad , \tag{71}$$

where the α_i are phase gradients and k is the wave number. The feed pattern for the cubic-lattice array is then:

$$E_{\mathcal{F}}(\theta, \phi) = F_o\, f_1 f_2 f_3 \tag{72}$$

where

$$f_s = \frac{\sin n_s\, \gamma_s/2}{\sin \gamma_s/2} e^{-i(ns-1)\gamma_s/2} \tag{73}$$

and F_o is the source element pattern. Equation 73 may be compared to equation 67, which was obtained by Fourier transform theory. The cubic-lattice notation permits imaging in a ground plane ($\alpha_3 = \pi$), but this capability is ordinarily defaulted ($\gamma_3 = 0$) when the source elements are electromagnetic horns. A rectangular feed aperture of discrete sources becomes available by this analysis.

Equation 72 may be regarded as a statement of the pattern multiplication principle or the result of time-domain convolution of a source distribution with an array factor distribution:

$$|E_{\mathcal{F}}(\theta, \phi)| = (F_o)(F_1 F_2 F_3) \quad . \tag{74}$$

The advantage of using equation 67 or its generalization (equation 73) instead of equation 25 is that there exists an inherent risk that the elliptical beams postulated by certain parameters (N_i, ϵ_i, β_i) of equation 25 may not be realizable in the physical world. There is a reduced risk when using equation 67, but unrealistic specifications are still possible. For example, t_o may be selected so small that the phase centers of the discrete sources could never be brought adequately close together even with radical dielectric loading. For Butler array-matrix simulations, the element spacing is usually set at one-half wavelength. The size of the array and its distance from the surface being illuminated must still be regarded to justify use of the preceding far-field radiation pattern equations for the prime feed in the simulation.

BEAM-FORMING MATRICES

The assumption of multiple beams having a common phase center has a basis in the physical world. Numerous beam-forming matrices exist (Ref. 23, Chapter 3, p. 217). The Butler array matrix is one that forms (n_s) orthogonal beams with a 4-dB crossover level, predicted on the array factor with half-wave separation between source elements. In systems simulation, it is convenient to express the properties of such a beam-forming device or circuit as a mathematical matrix. Scattering matrix notation may be adapted to transfer matrix notation, which admits chain matrix multiplication (Ref. 26, pp. 506-539). Computer processing for the circuit becomes a straightforward operation.

A four-port 90° (square) hybrid junction is the basic building block of the Butler matrix, together with certain fixed phase shifters. Transfer matrix notation and the noncommutative order of multiplication may be illustrated by a simple example for a lossless "weighting" circuit (Figure 32) whose output depends on a single phase shifter (ψ_1). The example is given in more general terms, including a second phase shifter (ψ_2) and making provision for a transmission coefficient. This is done since cascaded Butler matrices have been proposed with variable phase shifters interposed (Ref. 27). Also, an attempt is made to explore the proposition that the Butler array matrix is a Fourier transform device.

Figure 32 shows the "weighting" circuit with inputs h_1 and h_3, and outputs g_1 and g_3. The even-index quantities are absent because only the "transmit" submatrix of a partioned matrix is being considered here. Two null matrices and a "receive" matrix have been suppressed. The order of the matrices affecting the input signal is:

$$T_1 T_2 \cdots T_{n-1} T_n \tag{75}$$

so that the transfer matrix chain multiplication is carried out as:

$$\bar{g} = [T_n] [T_{n-1}] \cdots [T_1] \bar{h} \tag{76}$$

For the "weighting" circuit,

$$\begin{bmatrix} g_1 \\ g_3 \end{bmatrix} = \begin{bmatrix} -j/\sqrt{2} & -1/\sqrt{2} \\ -1/\sqrt{2} & -j/\sqrt{2} \end{bmatrix} \begin{bmatrix} \Gamma_1 e^{-j\psi_1} & o \\ o & \Gamma_2 e^{-j\psi_2} \end{bmatrix} \begin{bmatrix} -j/\sqrt{2} & -1/\sqrt{2} \\ -1/\sqrt{2} & -j/\sqrt{2} \end{bmatrix} \begin{bmatrix} h_1 \\ h_3 \end{bmatrix}$$

$$= \frac{1}{2} \begin{bmatrix} (-\Gamma_1 e^{-j\psi_1} + \Gamma_2 e^{-j\psi_2}) & (j\Gamma_1 e^{-j\psi_1} + j\Gamma_2 e^{-j\psi_2}) \\ (j\Gamma_1 e^{-j\psi_1} + j\Gamma_2 e^{-j\psi_2}) & (\Gamma_1 e^{-j\psi_1} - \Gamma_2 e^{-j\psi_2}) \end{bmatrix} \begin{bmatrix} h_1 \\ h_3 \end{bmatrix} \quad (77)$$

Defaulting the result, set Γ_1 equal to Γ_2 equal to unity, and ψ_1 equal to ψ_2 equal to zero. Then,

$$\begin{bmatrix} g_1 \\ g_3 \end{bmatrix} = \begin{bmatrix} o & j \\ j & o \end{bmatrix} \begin{bmatrix} h_1 \\ h_3 \end{bmatrix} = \begin{bmatrix} jh_3 \\ jh_1 \end{bmatrix} \quad (78)$$

It can be seen that the magnitudes of outputs (g_1 and g_3 are the inputs h_3 and h_1, respectively). This is a symmetry argument. Since a single square hybrid is an elementary Butler matrix, cascading two such hybrids might constitute "transform of a transform" in the Fourier sense.

The proposition that a Butler matrix is a Fourier transform device is difficult to support formally for the two-port example shown here, or for the n_s-port matrix, even though additional properties associated with a Fourier transform emerge. Suppose only a single hybrid is considered, so that:

$$\begin{bmatrix} g_1 \\ g_3 \end{bmatrix} = \frac{-1}{\sqrt{2}} \begin{bmatrix} j & 1 \\ 1 & j \end{bmatrix} \begin{bmatrix} h_1 \\ h_3 \end{bmatrix} \quad (79)$$

Suppose further that h_3 is identically zero, initially. Then it is possible to write

$$g_1 = \frac{-1}{\sqrt{2}} e^{j\pi/2} \quad (80)$$

and

$$g_3 = \frac{-1}{\sqrt{2}} e^{jo} \quad (81)$$

Now the single input (h_1) equal to unity may be regarded as a delta-function and (ft_o) may be taken to equal minus one-fourth for g_1 and zero for g_3, so that:

$$\mathcal{F}[\delta(t - t_o)] = e^{-j2\pi ft_o} \quad (82)$$

reproduces the exponentials of equations 80 and 81 above. This has the appearance of annexing the frequency-shifting property of Fourier transform theory to the symmetry property. It is noted, however, that the Butler matrix of n_s output ports accepts a single input, $\delta(t - t_o)$ and produces a

discrete set of output values $e^{-j2\pi f_1 t_o}, e^{-j2\pi f_2 t_o}, \ldots, e^{-j2\pi f n_s t_o}$, whereas equation 82 indicates a continuous output. The discrete set of values may well be bounded by equation 82, but the proposition regarding the Butler array matrix as a Fourier transform device appears to be restricted.

TRANSFER MATRICES

Admitting the possibility of a restriction regarding the Butler array matrix as a Fourier transformer, the requisite signal processing may still be carried out conveniently using the preceding transfer matrix notation. In view of certain publications, including Reference 27, and the experience gained in the present effort, a transfer function consisting of three matrices would be useful in the development of future computer programs. The cascading of Butler matrices or power dividers of different dimension is anticipated. A single transfer function that accommodates these options may be written. Matrix conformability problems regarding Butler matrix dimensionality are circumvented by an artifice. The higher dimension is carried throughout, certain parameters are defaulted, and the matrix of smaller dimension is thereby imbedded in the formulation.

The circuit of Figure 33 cascades Butler matrices of dimension equal to eight and four. Notation is the same for the square hybrid example, previously given, as is the order of multiplication. An equivalent matrix for the entire transfer function may be obtained by multiplication:

$$[T_{eq}] = [T_3]\,[T_2]\,[T_1] \tag{83}$$

where $[T_1]$ is associated with a four-beam array matrix or power divider, $[T_2]$ designates a bank of "weighted" phase shifters, and $[T_3]$ is associated with an eight-beam array matrix. Prior to defaulting any of the parameters,

$$\begin{bmatrix} g_1 \\ g_3 \\ g_5 \\ g_7 \\ g_9 \\ g_{11} \\ g_{13} \\ g_{15} \end{bmatrix} = \frac{1}{\sqrt{8}} \begin{bmatrix} T_{11} & T_{12} & T_{13} & T_{14} & T_{15} & T_{16} & T_{17} & T_{18} \\ T_{21} & T_{22} & T_{23} & T_{24} & T_{25} & T_{26} & T_{27} & T_{28} \\ T_{31} & T_{32} & T_{33} & T_{34} & T_{35} & T_{36} & T_{37} & T_{38} \\ T_{41} & T_{42} & T_{43} & T_{44} & T_{45} & T_{46} & T_{47} & T_{48} \\ T_{51} & T_{52} & T_{53} & T_{54} & T_{55} & T_{56} & T_{57} & T_{58} \\ T_{61} & T_{62} & T_{63} & T_{64} & T_{65} & T_{66} & T_{67} & T_{68} \\ T_{71} & T_{72} & T_{73} & T_{74} & T_{75} & T_{76} & T_{77} & T_{78} \\ T_{81} & T_{82} & T_{83} & T_{84} & T_{85} & T_{86} & T_{87} & T_{88} \end{bmatrix} \begin{bmatrix} T_{11} & 0 & 0 & 0 & 0 & 0 & 0 & 0 \\ 0 & T_{22} & 0 & 0 & 0 & 0 & 0 & 0 \\ 0 & 0 & T_{33} & 0 & 0 & 0 & 0 & 0 \\ 0 & 0 & 0 & T_{44} & 0 & 0 & 0 & 0 \\ 0 & 0 & 0 & 0 & T_{55} & 0 & 0 & 0 \\ 0 & 0 & 0 & 0 & 0 & T_{66} & 0 & 0 \\ 0 & 0 & 0 & 0 & 0 & 0 & T_{77} & 0 \\ 0 & 0 & 0 & 0 & 0 & 0 & 0 & T_{88} \end{bmatrix} \frac{1}{2} \begin{bmatrix} 2 & 0 & 0 & 0 & 0 & 0 & 0 & 0 \\ 0 & 2 & 0 & 0 & 0 & 0 & 0 & 0 \\ 0 & 0 & T_{33} & T_{34} & T_{35} & T_{36} & 0 & 0 \\ 0 & 0 & T_{43} & T_{44} & T_{45} & T_{46} & 0 & 0 \\ 0 & 0 & T_{53} & T_{54} & T_{55} & T_{56} & 0 & 0 \\ 0 & 0 & T_{63} & T_{64} & T_{65} & T_{66} & 0 & 0 \\ 0 & 0 & 0 & 0 & 0 & 0 & 2 & 0 \\ 0 & 0 & 0 & 0 & 0 & 0 & 0 & 2 \end{bmatrix} \begin{bmatrix} h_1 \\ h_3 \\ h_5 \\ h_7 \\ h_9 \\ h_{11} \\ h_{13} \\ h_{15} \end{bmatrix} \tag{84}$$

$(\bar{g})$ (T_3) (T_2) (T_1) $(\bar{h})$

Assume that

$$h_1 = h_3 = h_{13} = h_{15} = 0 \tag{85}$$

for the coma correction circuit. For the remaining inputs, assume that only h_5 is nonzero initially. It can be seen that product $[T_1]\,[\bar{h}]$ results in a column vector (or matrix). The elements T_{33}, T_{43}, T_{53}, and T_{63} of $[T_1]$ are exponential terms of the stepwise linear phase gradient that is ordinarily associated with an "antenna beam" from this Butler matrix.

Multiplying column vector $[T_1]$ [h] against matrix $[T_2]$, in the order indicated, introduces elements T_{33}, T_{44}, T_{55}, and T_{66} of $[T_2]$. The elements are weighted exponentials whose arguments are such that they remove the linear gradient due to $[T_1]$ and the comatic aberration as well. The weighting factors provide the amplitude taper of the elliptical beams of the previous discussion. Symmetric taper of the feed function alone is obtained with $[T_{33}]$ equal to $[T_{66}]$ and $[T_{44}]$ = $[T_{55}]$ in matrix $[T_2]$ in the present discussion. Product $[T_2]$ $[T_1]$ [h] results in another column vector that, when multiplied against matrix $[T_3]$, leads to four antenna beams. Each beam is associated with a column of matrix $[T_3]$ as indicated in equation 84.

CONCLUSION

This document developed analytical/numerical approaches to identifying and correcting the aberrations introduced by a general displacement of the feed from the focal point of a single offset paraboloid antenna used in radiometer systems. The transmit point of view led to an optical path difference in the aperture plane. Classical aberration theory was then applied in an attempt to determine the mathematical composition of the optical path difference or total aberration. It was noted that the classical theory was useful, but large feed displacements and the inclusion of an asymmetrical antenna surface caused the investigation to depart from Gaussian optics and violate Hamilton's assumption of a symmetrical instrument. No attempt was made to include the effects of apodization or amplitude taper in the geometric analysis here.

Ray optics was also applied with the receive point of view, leading to the development of wavefronts and caustics, under the assumption of zero wavelength. This approach was augmented with the physical optics mapping of the focal-region fields at a wavelength of 0.212 meter to determine suitable feed positions for a given plane-wave angle of arrival.

Finally, physical optics was used for the transmit case to compute far-field radiation patterns and to test various hypotheses. A common phase center was assumed for a prime feed that radiated five elliptical beams. Both phase and amplitude taper were used in a mathematical simulation that is also physically realizable. The prime feed was associated with the Butler array matrix and its constraints. It was found that the quality of coma correction was set by feed size (number of discrete sectors on the reflector), and adverse effects orthogonal to the comatic phase gradient. Beam-scan angle (projected aperture) determined minimum beamwidth.

This document illustrates some of the methods that may be applied in future radiometric antenna design effort and points out limitations of those methods. The actual coma correction achieved in the various examples is considered incidental to the value of the methods discussed. Mapping of the aberration coefficients for parent and offset paraboloids has not been found in the open literature, and appears to provide useful insight for the coma-correction problem and other antenna studies. A modified aperture-plane analysis for complex distributions, combined with a Fast Fourier Transform (FFT) capability, could replace the physical-optics approach used in the present effort. The inclusion of transfer matrices is not imperative, but constitutes a useful alternative in an automated approach to coma correction. Finally, it appears that coma correction remains an art, rather than a science, since the computational path is very long. There are many variables and constraints;

cause and effect cannot be expressed in any simple manner. An iterative approach appears to be necessary.

ACKNOWLEDGMENTS

The author is indebted to Raymons Miezis, who developed the code for the physical-optics and ray-trace programs used herein, and to Yeak-Laan (Janet) Chien, who subsequently applied the programs and provided the polynomial approximation to the aperture-plane aberration data.

Page Intentionally Left Blank

REFERENCES

1. Silver, S. (Ed.), *Microwave Antenna Theory and Design*, McGraw-Hill Book Company, Inc., 1949.

2. Cornbleet, S., *Microwave Optics*, Academic Press, 1976.

3. O'Neill, E. L., *Introduction to Statistical Optics*, Addison-Wesley Publishing Co., Inc., 1963.

4. Wolfe, W. L., "The Infrared Handbook," Environmental Research Institute of Michigan, Lib. Congress Cat. Card No. 77-90786, 1978.

5. Rudge, A. W., and M. J. Withers, "New Technique for Beam Steering with Fixed Parabolic Reflectors," *Proc. IEE*, 118(7), July 1971.

6. Welford, W. T., *Aberrations of the Symmetrical Optical System*, Academic Press, 1974.

7. Linfoot, E. H., *Recent Advances in Optics*, Oxford, 1955.

8. Born, M., and E. Wolf, *Principles of Optics*, Pergamon Press, 1964.

9. Herzberger, M., *Modern Geometrical Optics*, Interscience Publishers, Inc., 1958.

10. Kline, M., and I. W. Kay, *Electromagnetic Theory and Geometrical Optics*, Interscience Publishers, Inc., 1965.

11. Stavroudis, O. N., *The Optics of Rays, Wavefronts, and Caustics*, Academic Press, 1972.

12. Schmidt, R. F., "Principal Normal Curvature of Surfaces," NASA TM-82102, March 1981.

13. Stalzer, H. J., Jr., "Comment on the Caustic Curve of a Parabola," *Applied Optics*, 4(9), September 1965.

14. Scarborough, J. B., "The Caustic Curve of an Off-Axis Parabola," *Applied Optics*, 3(12), December 1964.

15. Parke, D. M., "Calculation of the Caustic (Focal) Surface When the Reflecting Surface is a Paraboloid of Revolution and the Incoming Rays are Parallel," Parke Mathematical Laboratories, Inc., Contract AF 19(122)484, Air Force Cambridge Research Laboratories, February 15, 1952.

16. Bracewell, R., *The Fourier Transform and Its Applications*, McGraw-Hill Book Company, 1965.

17. Birkhoff, G., and S. MacLane, *A Survey of Modern Algebra*, The MacMillan Company, 1953.

18. Morse, P. M., and H. Feshbach, *Methods of Theoretical Physics*, McGraw-Hill Book Company, 1953.

19. Schmidt, R. F., "Quaternion Rotations Applied in Antenna Theory," Goddard Space Flight Center Technical Document X-811-77-285, December 1977.

20. Brigham, E. O., *The Fast Fourier Transform*, Prentice-Hall, Inc., 1974.

21. Hsu, H. P., *Fourier Analysis*, Simon and Schuster, 1970.

22. Butler, J., and R. Lowe, "Electronic Design," April 12, 1961.

23. Hansen, R. C., *Microwave Scanning Antennas, Volume III*, Academic Press, 1966.

24. Gaskill, J. D., *Linear Systems, Fourier Transforms, and Optics*, John Wiley and Sons, 1978.

25. Stratton, J. A., *Electromagnetic Theory*, McGraw-Hill Book Company, Inc., 1941.

26. Lax, B., and K. Button, *Microwave Ferrites and Ferrimagnetics*, McGraw-Hill Book Company, 1962.

27. Hung, C., and G. Chadwick, "Corrected Off-Axis Beams for Parabolic Reflectors," *IEEE/APS Symposium*, June 1979.

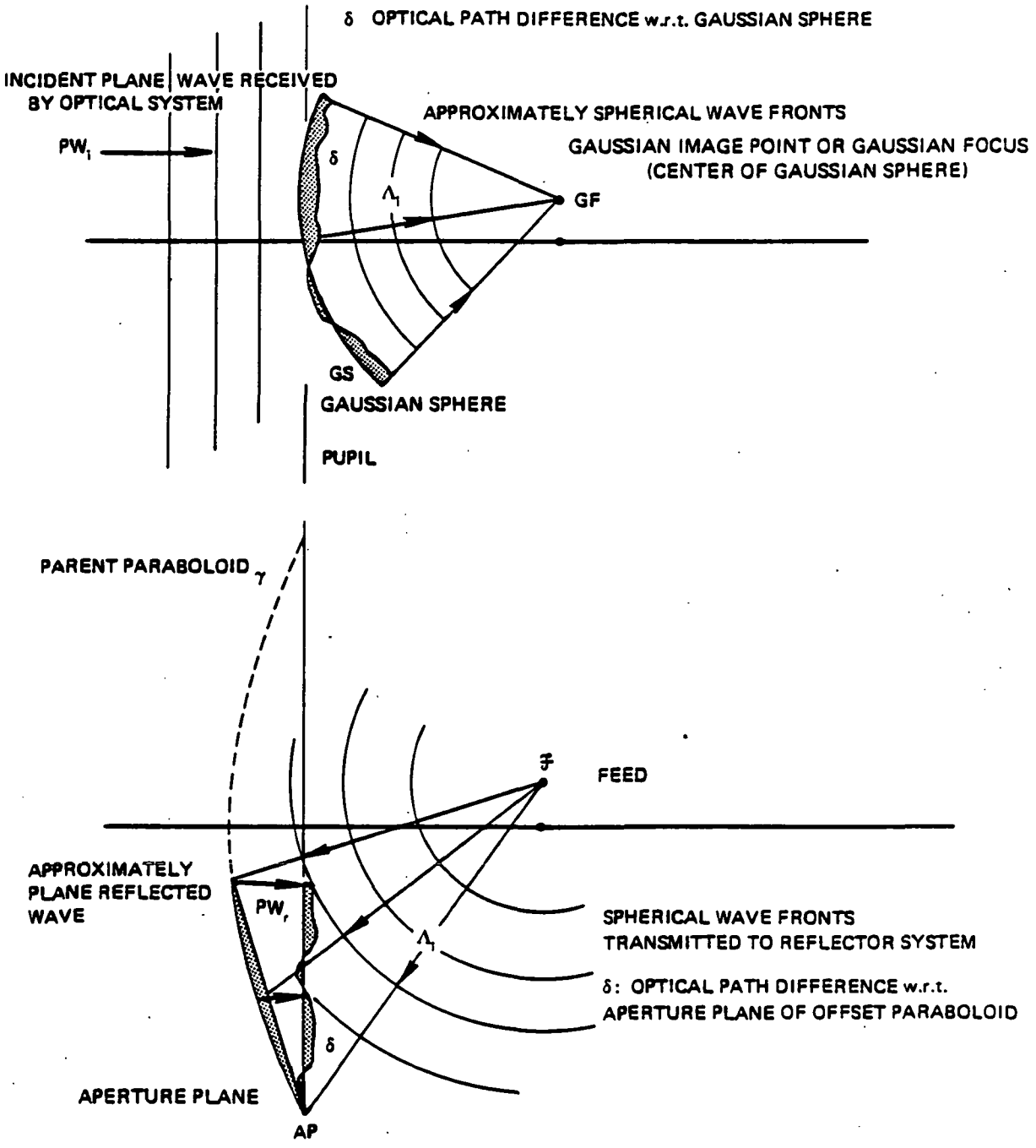

Figure 1. The optical path difference (OPD) for optical (receive)/microwave (transmit) views.

COORDINATES ON PARENT PARABOLOID:

$X_P = \sigma_{\ell P} \sin \zeta_{\ell P} + X_{1P}$ $\quad X_{1P} = -10.5$ m

$Y_P = -\sigma_{\ell P} \cos \zeta_{\ell P} + Y_{1P}$ $\quad Y_{1P} = 0.0$ m

$Z_P = \frac{\sigma_P 2}{4F} + Z_{1P}$ $\quad z_{1P} = -F = -18.0$ m

$\sigma_P{}^2 = X_P{}^2 + Y^2{}_P$

F/Dp = 0.5

F/Do = 1.2

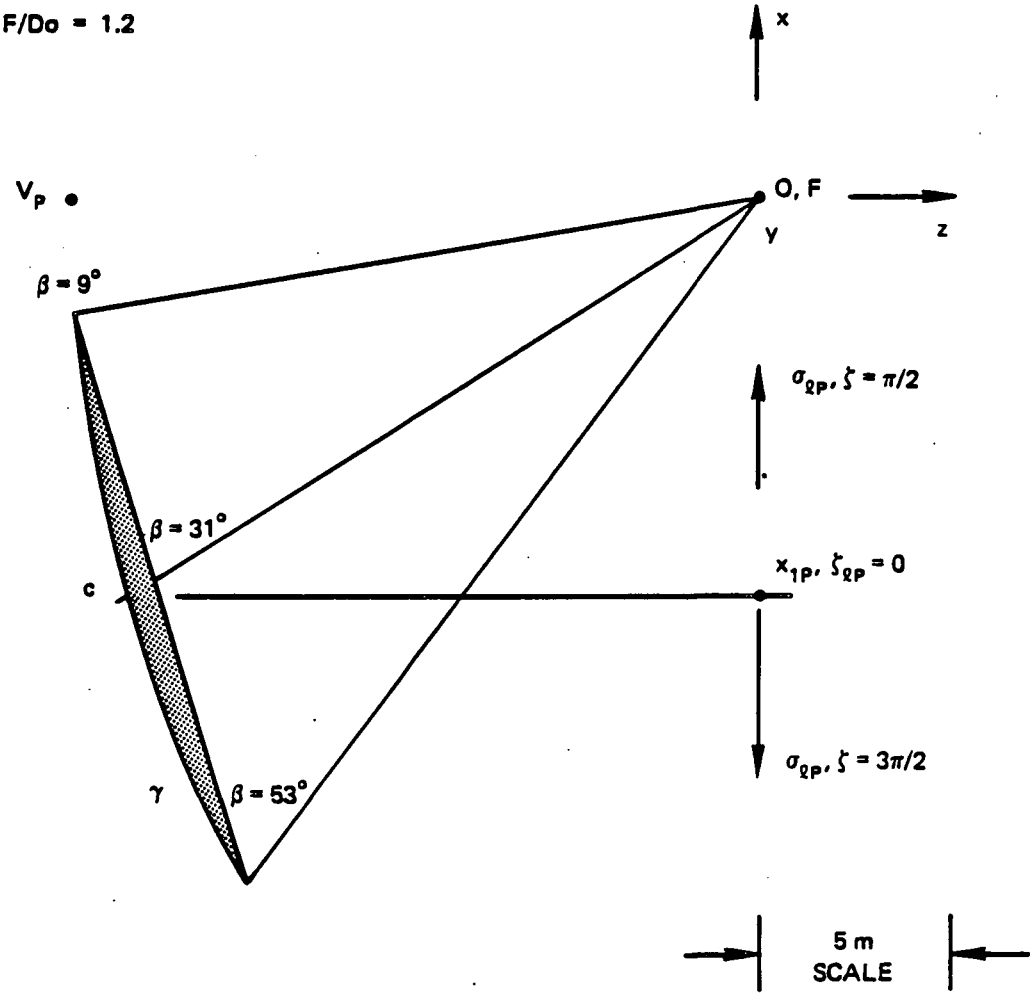

Figure 2. Geometry of the offset paraboloid.

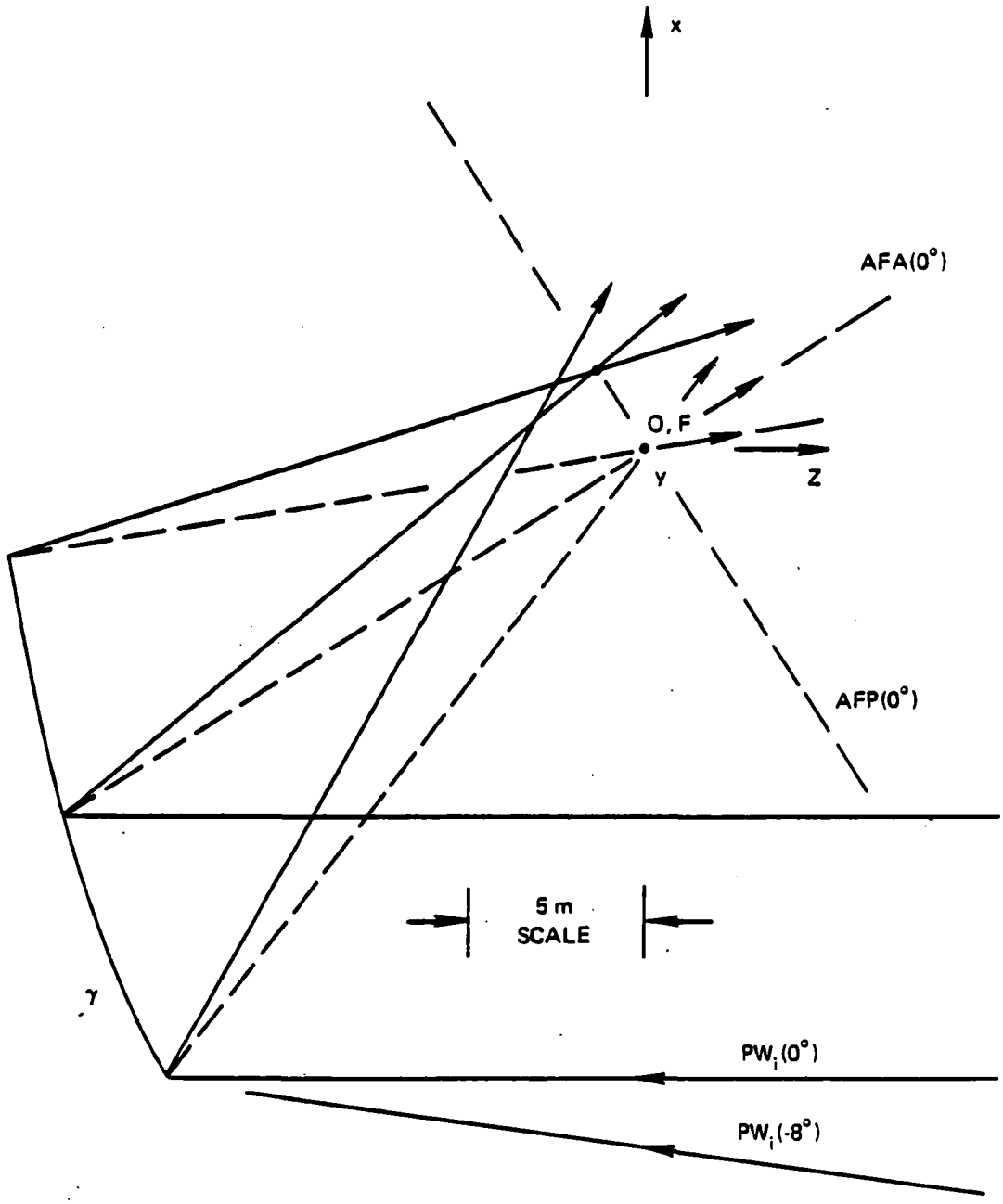

Figure 3. Three-ray trace for -8° plane-wave incidence (offset paraboloid).

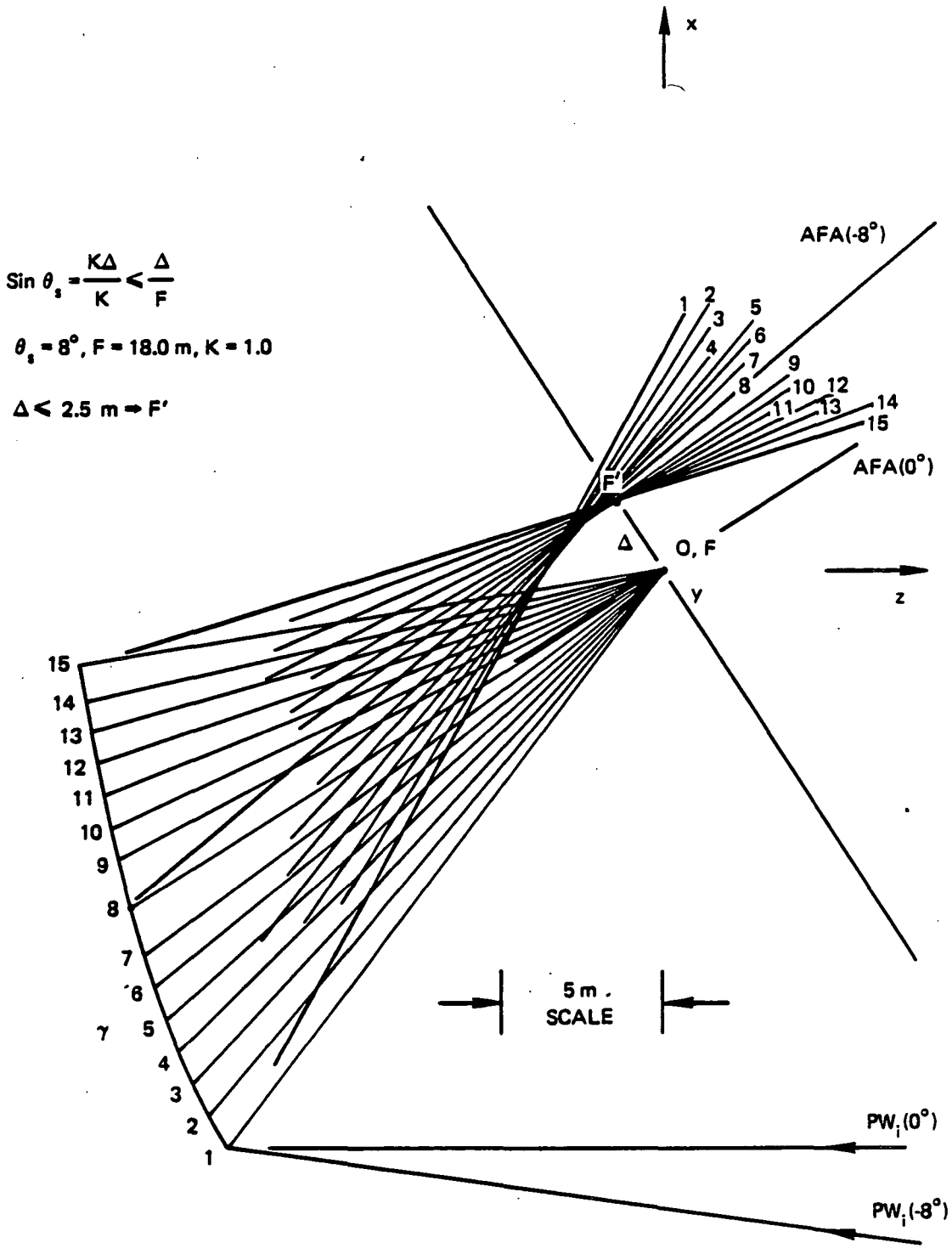

Figure 4. Envelope of caustic arc for -8° plane-wave incidence (offset paraboloid).

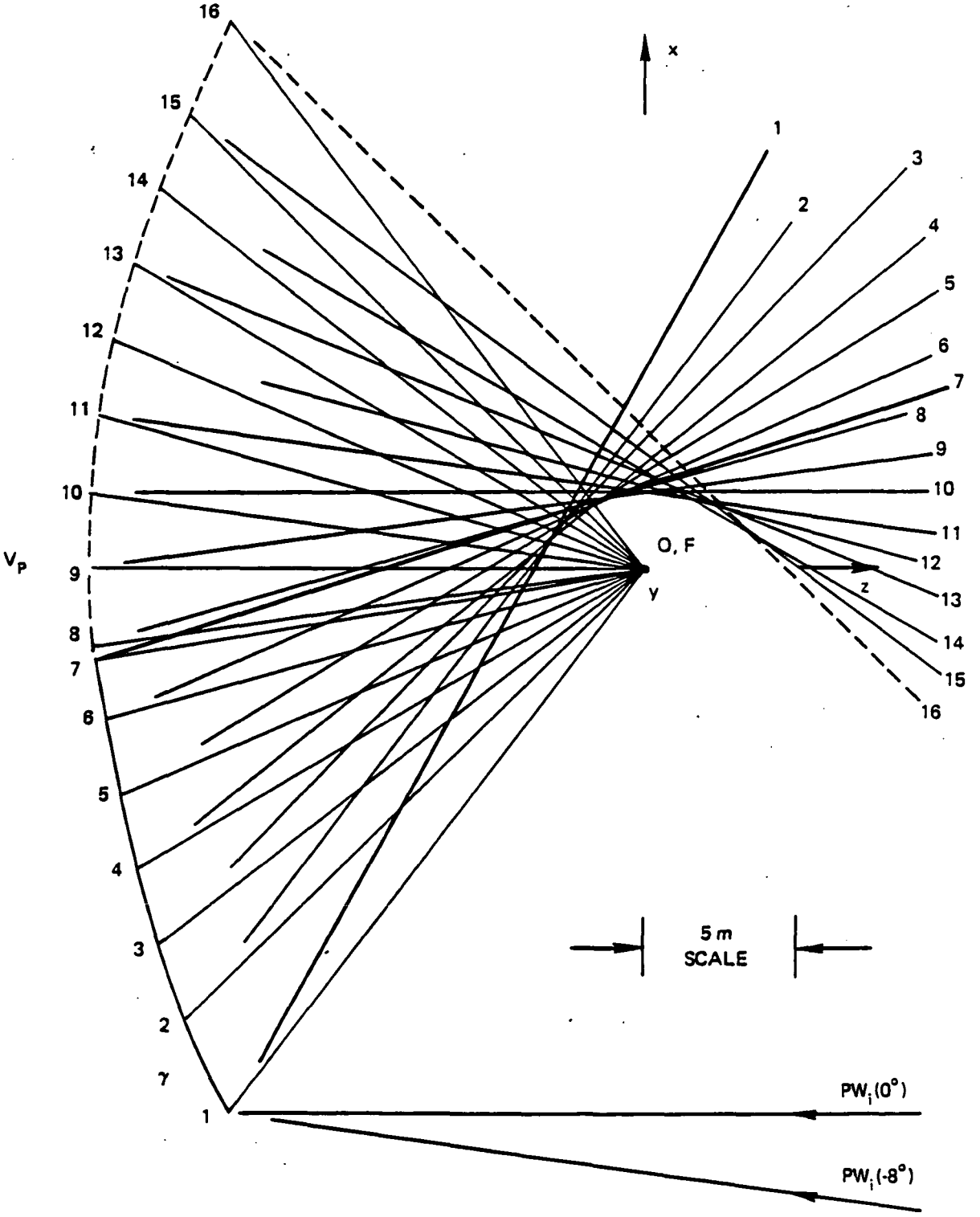

Figure 5. Envelope of caustic arc for -8° plane-wave incidence (parent and offset paraboloid).

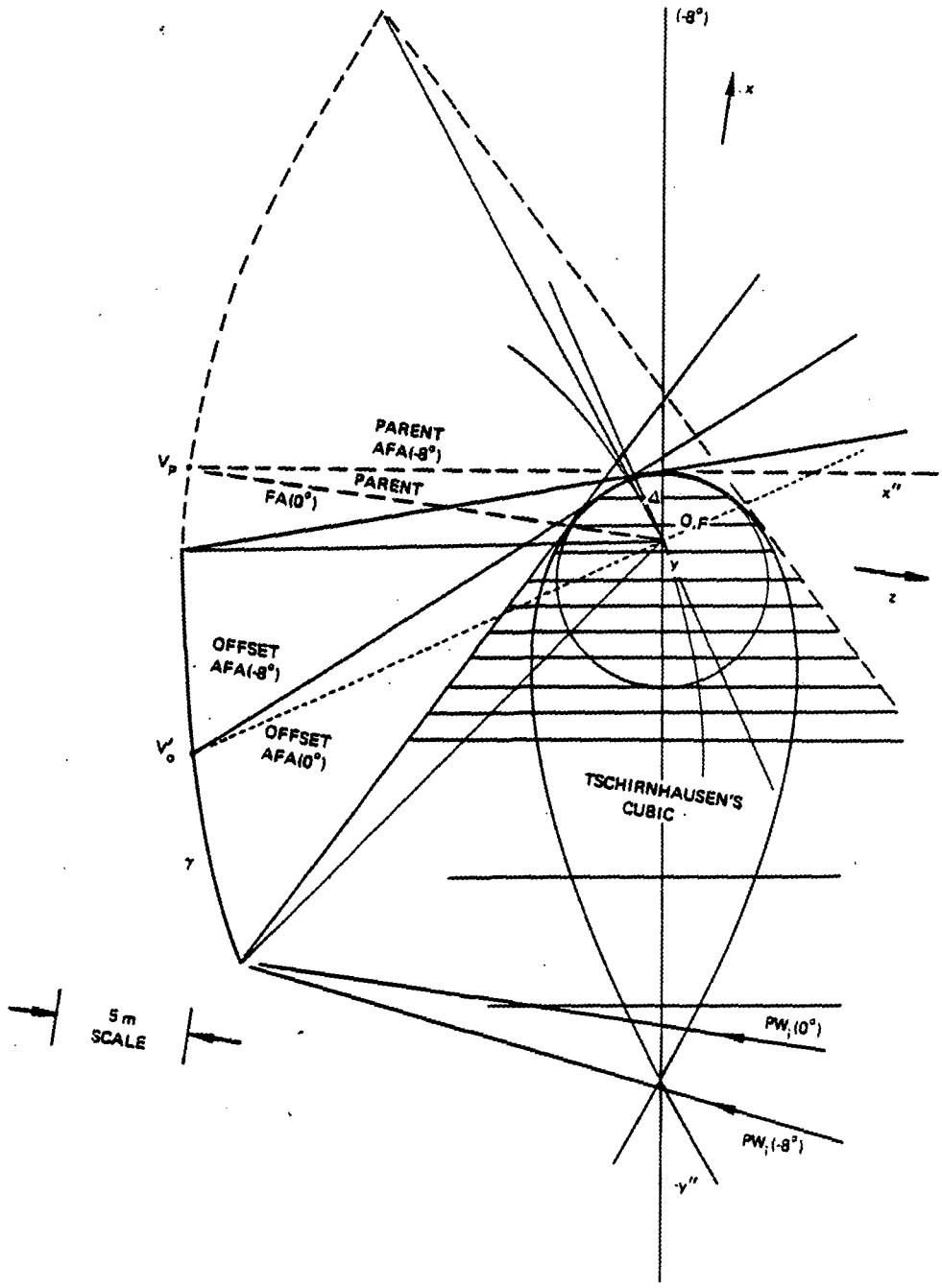

Figure 6. Analytical caustic curve for -8° plane-wave incidence (parent and offset paraboloid).

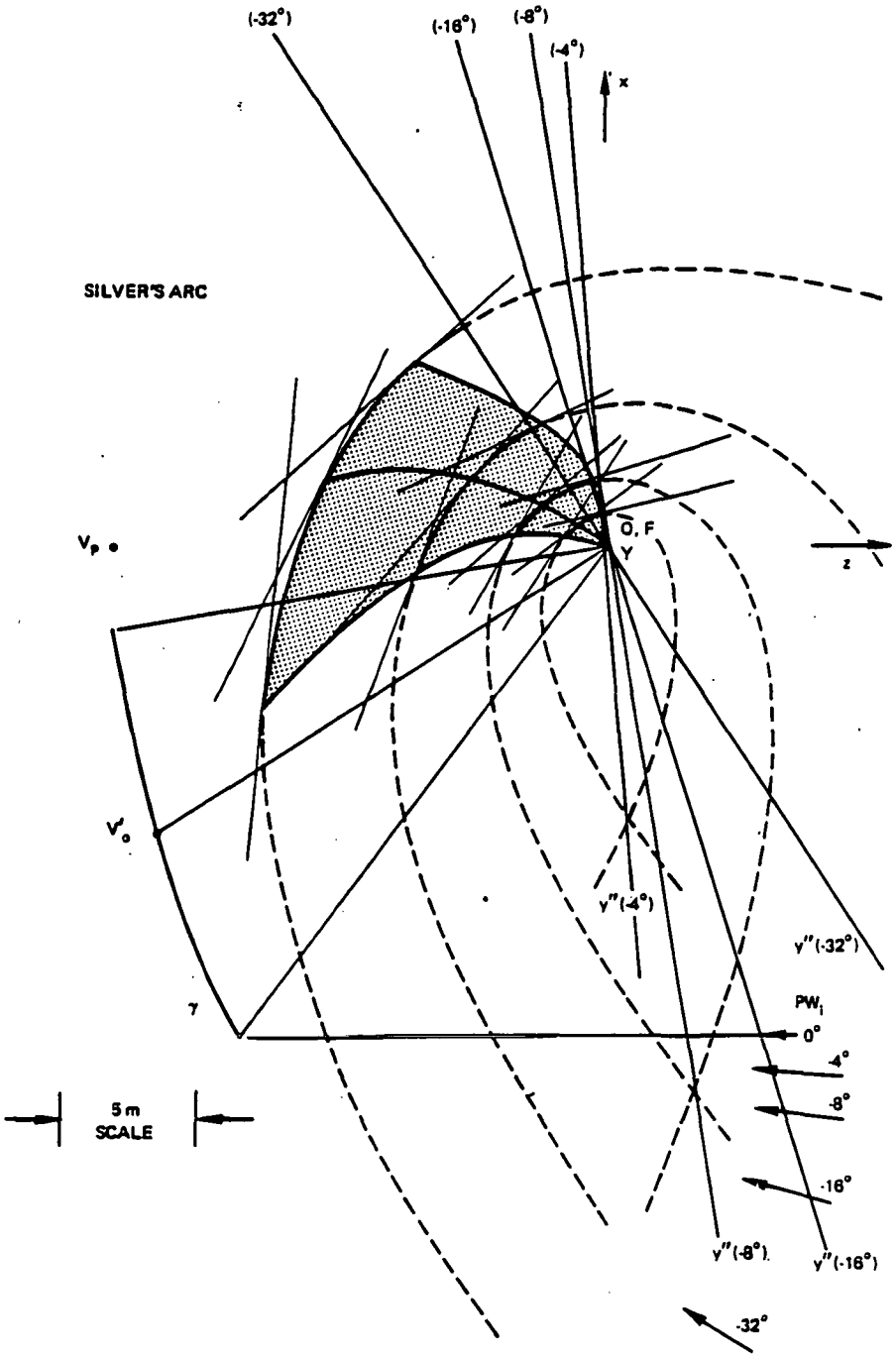

Figure 7. Truncated analytical caustic curve (Tschirnhausen's cubic) for -4°, -8°, -16°, and -32° plane-wave incidence (offset paraboloid).

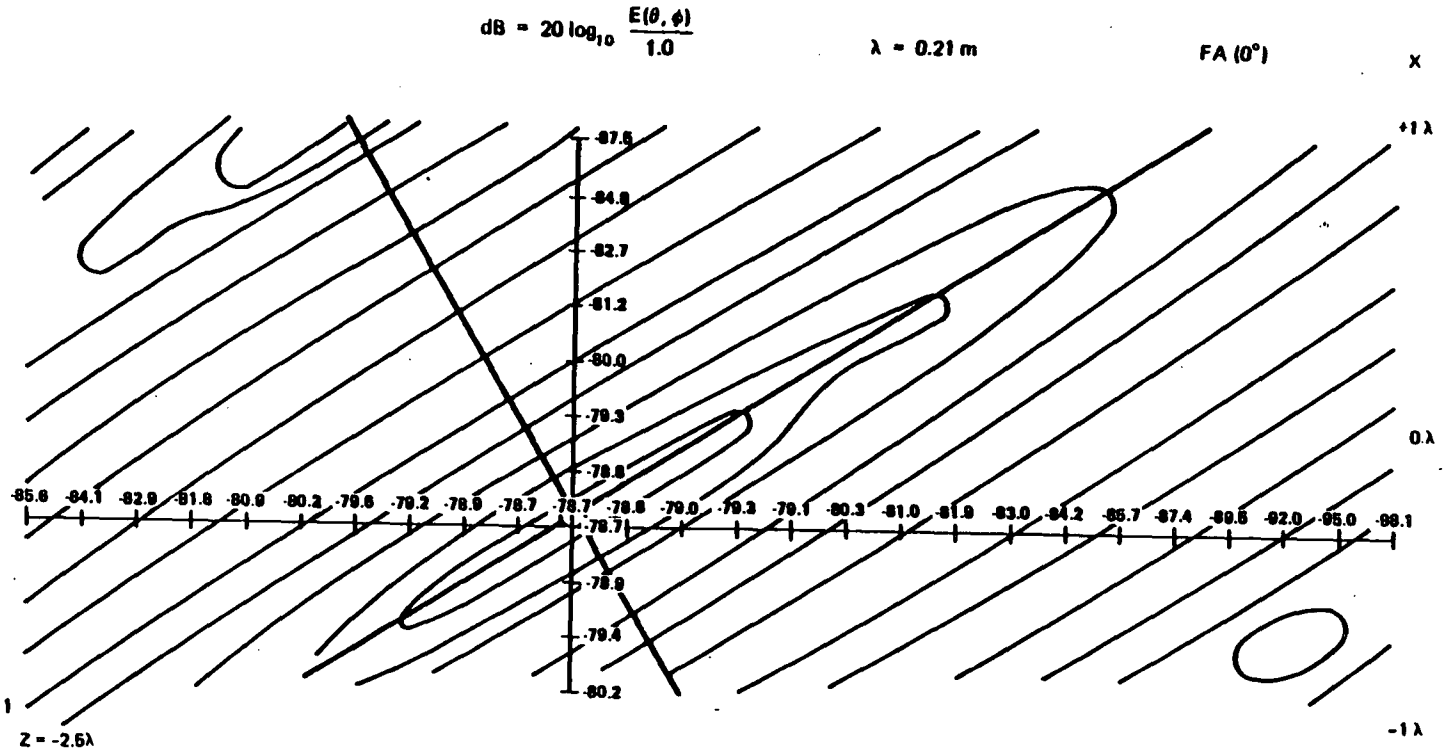

Figure 8. Focal-region map of offset paraboloid for axial plane-wave incidence.

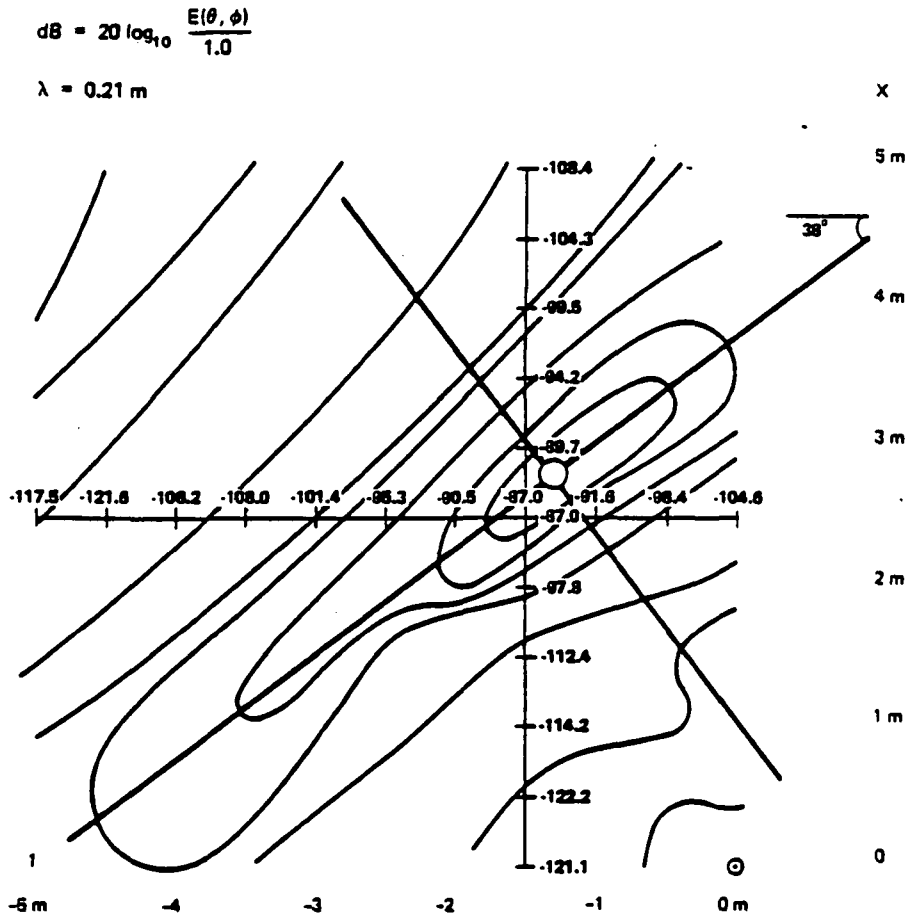

Figure 9. Focal-region map of offset paraboloid for -8.7° plane-wave incidence.

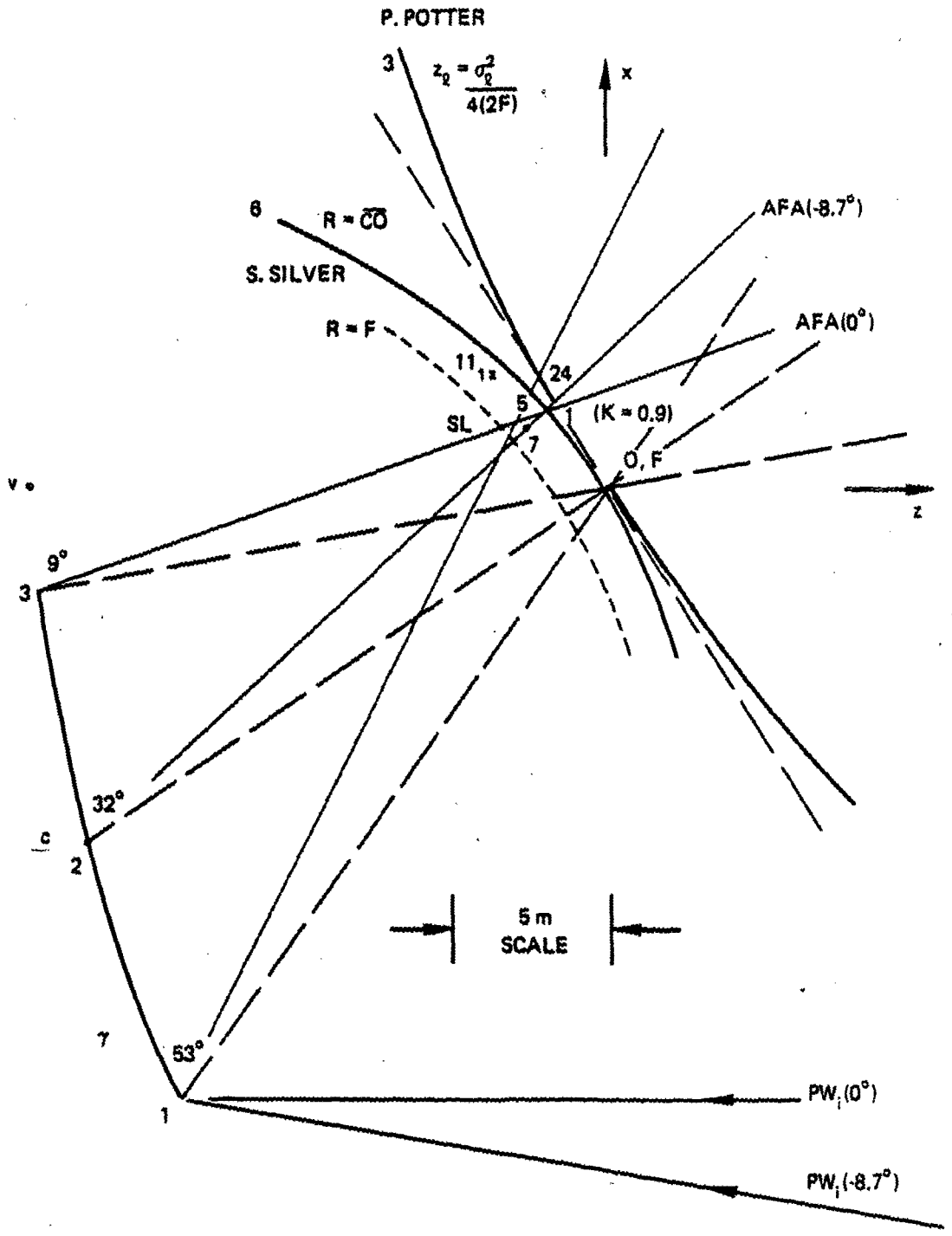

Figure 10. Estimates of the displaced and diffuse focus (F') for -8.7° plane-wave incidence.

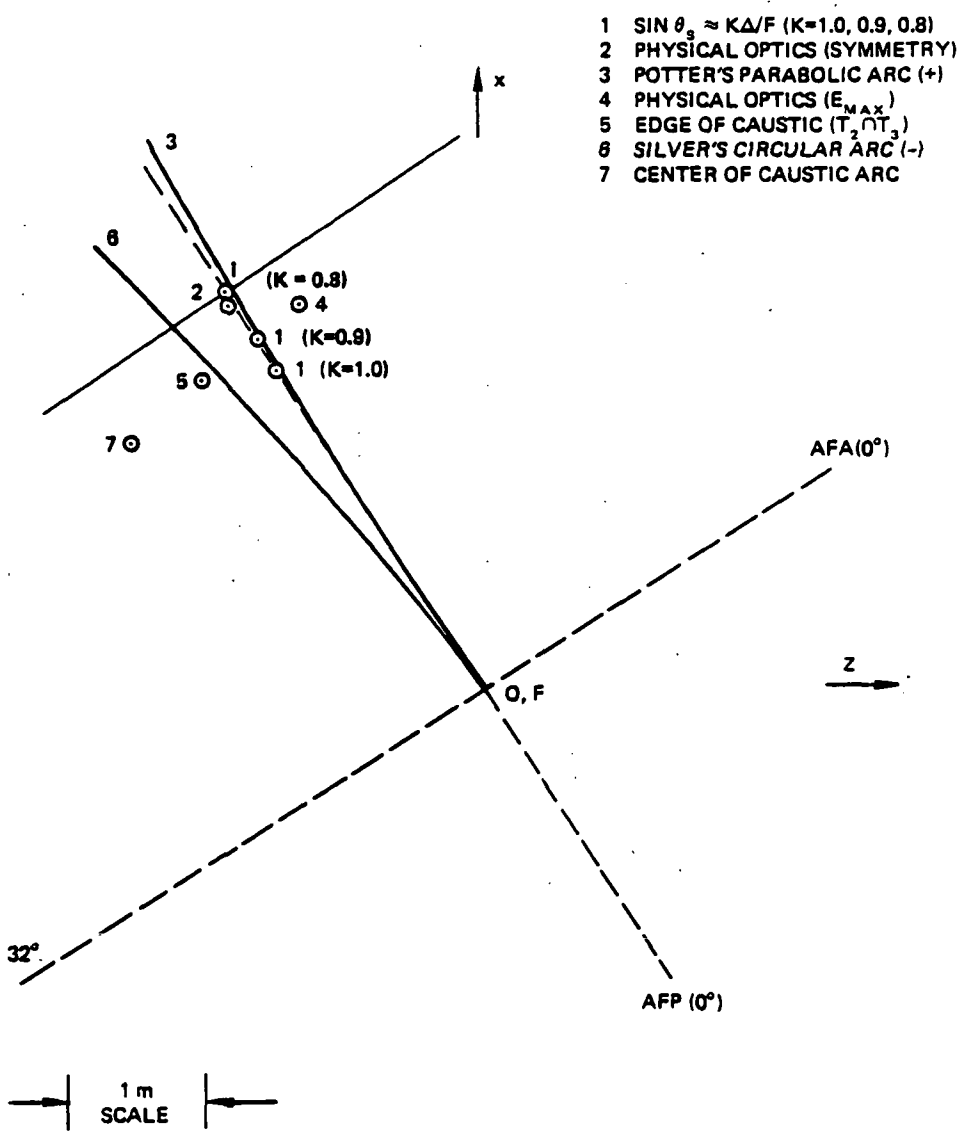

Figure 11. Coordinates [$\bar{\rho}_e = (x_e, y_e, z_e)$] of displaced focus (F') for -8.7° plane-wave incidence.

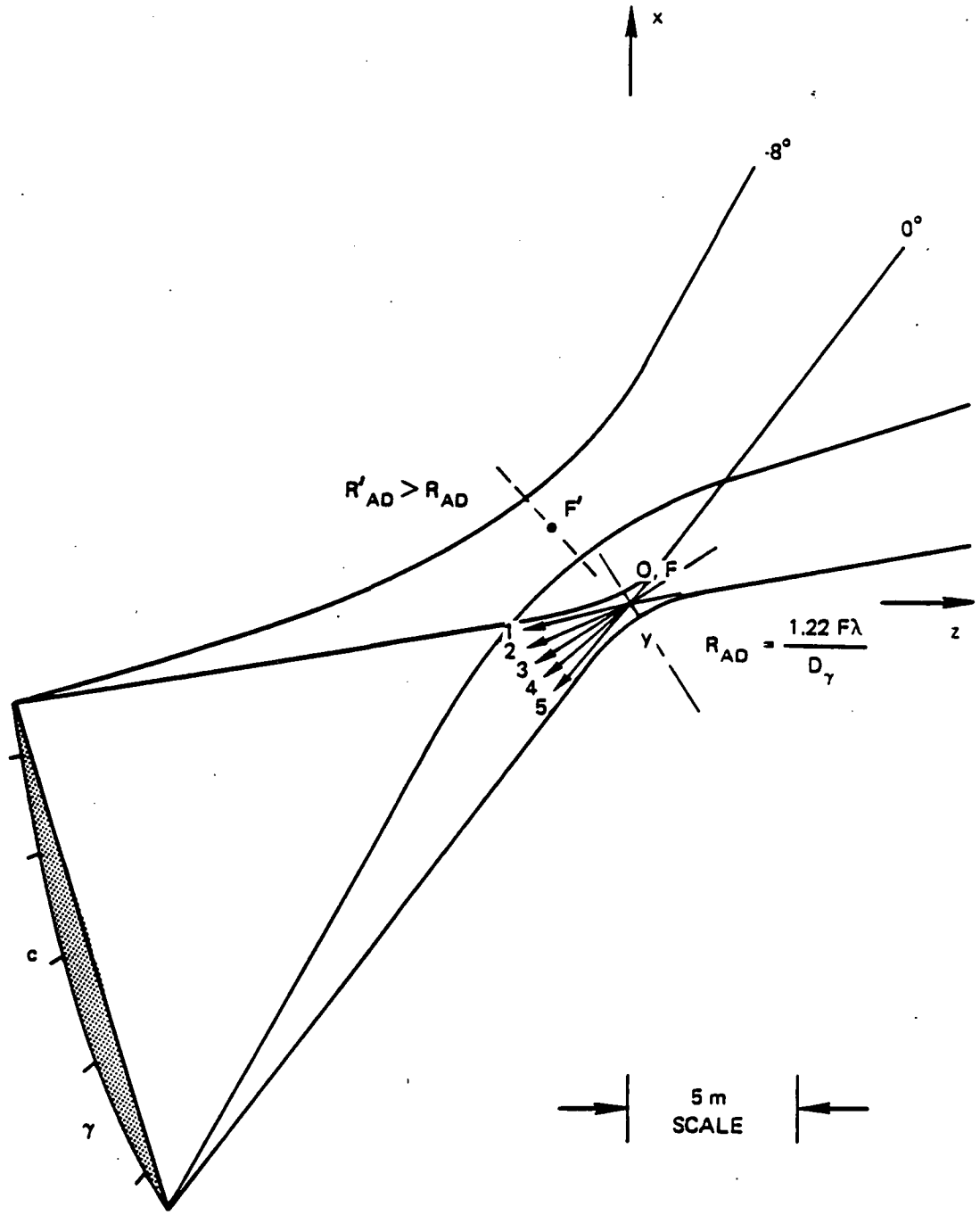

Figure 12. Offset paraboloid illumination of 0° and -8° plane-wave incidence showing displaced Airy discs.

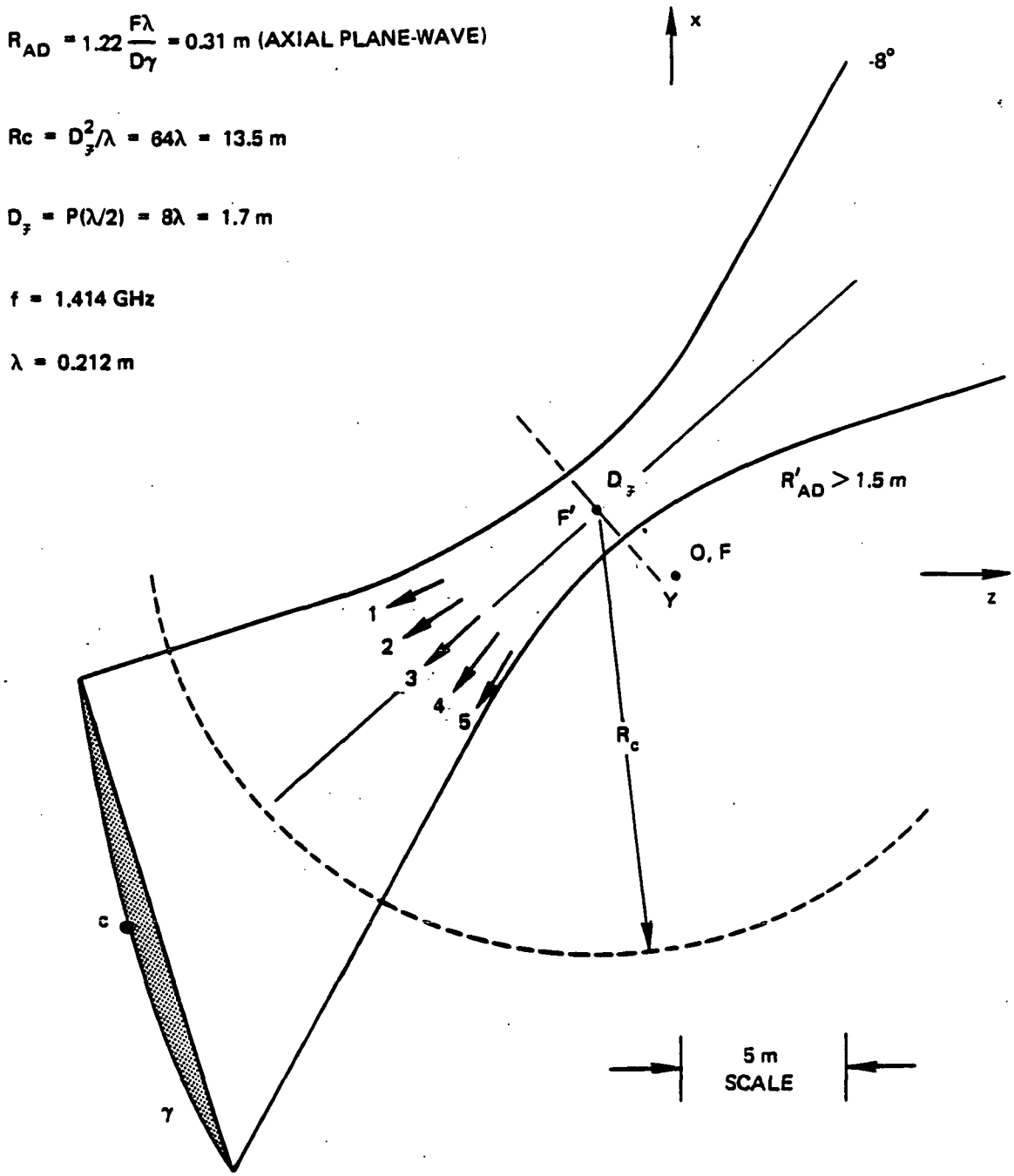

Figure 13. Offset paraboloid illumination of -8° plane-wave incidence showing feed (D_f) and far-field radius (R_c).

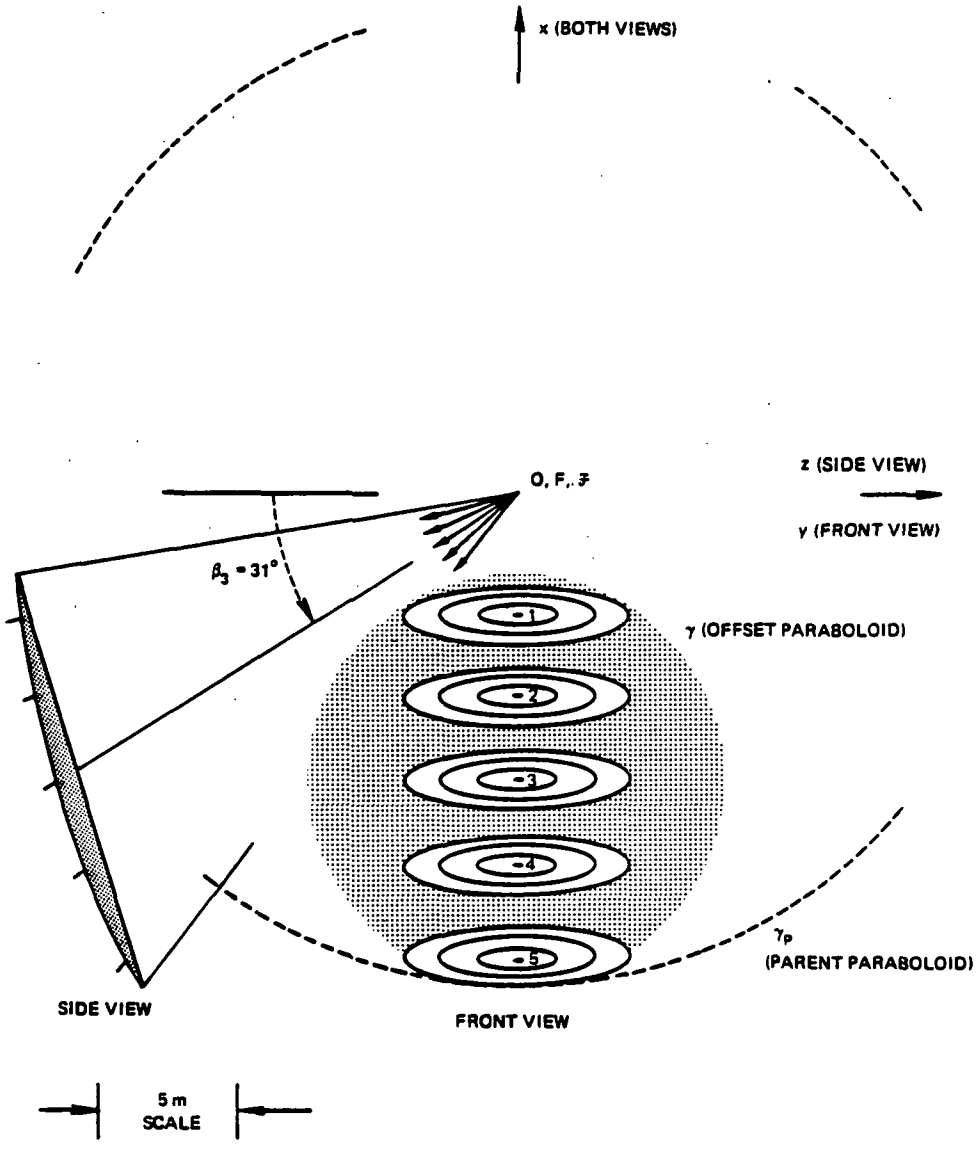

Figure 14. Illumination of offset paraboloid with five beams (i = 5).

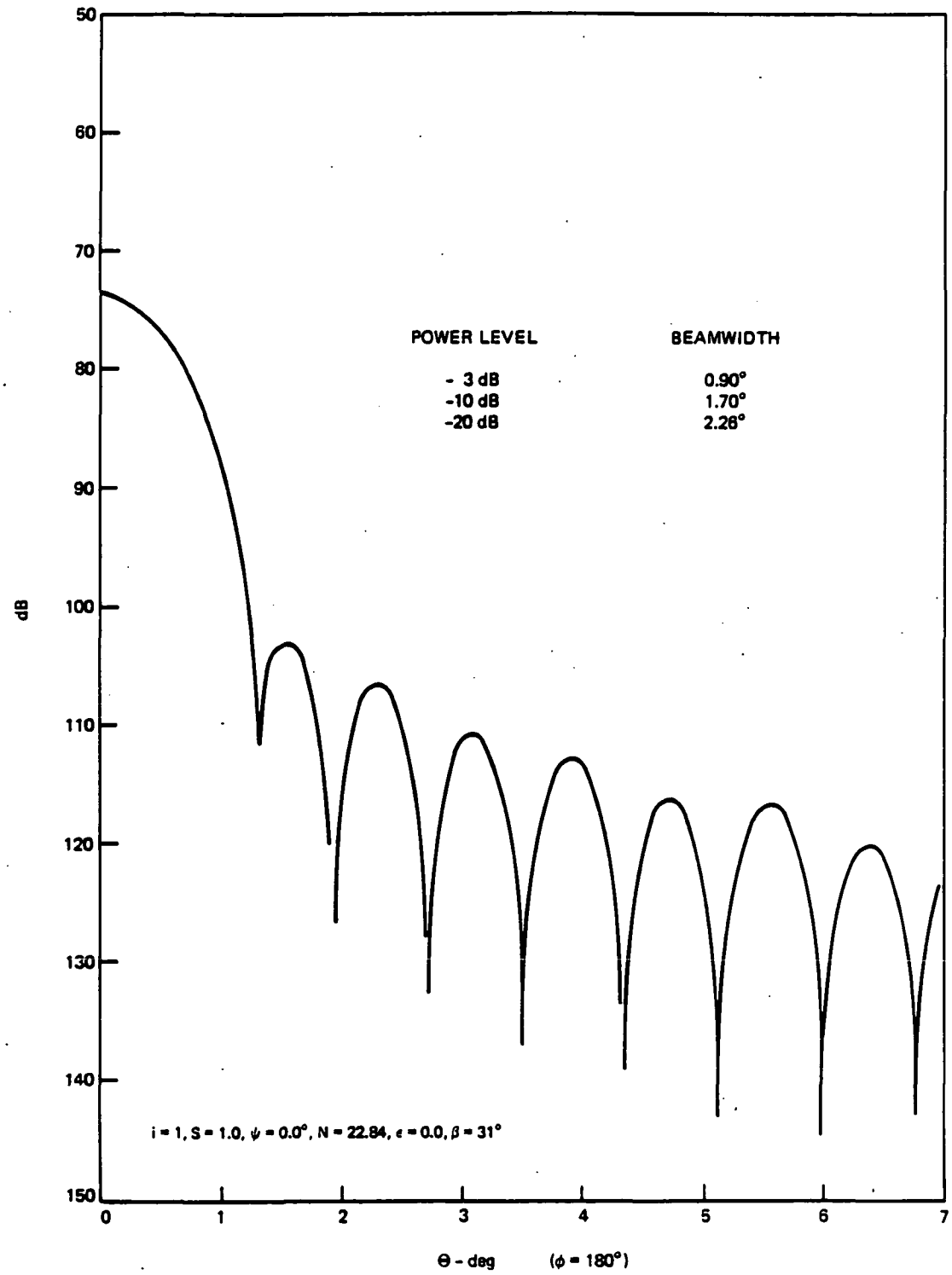

Figure 15. Reference pattern.

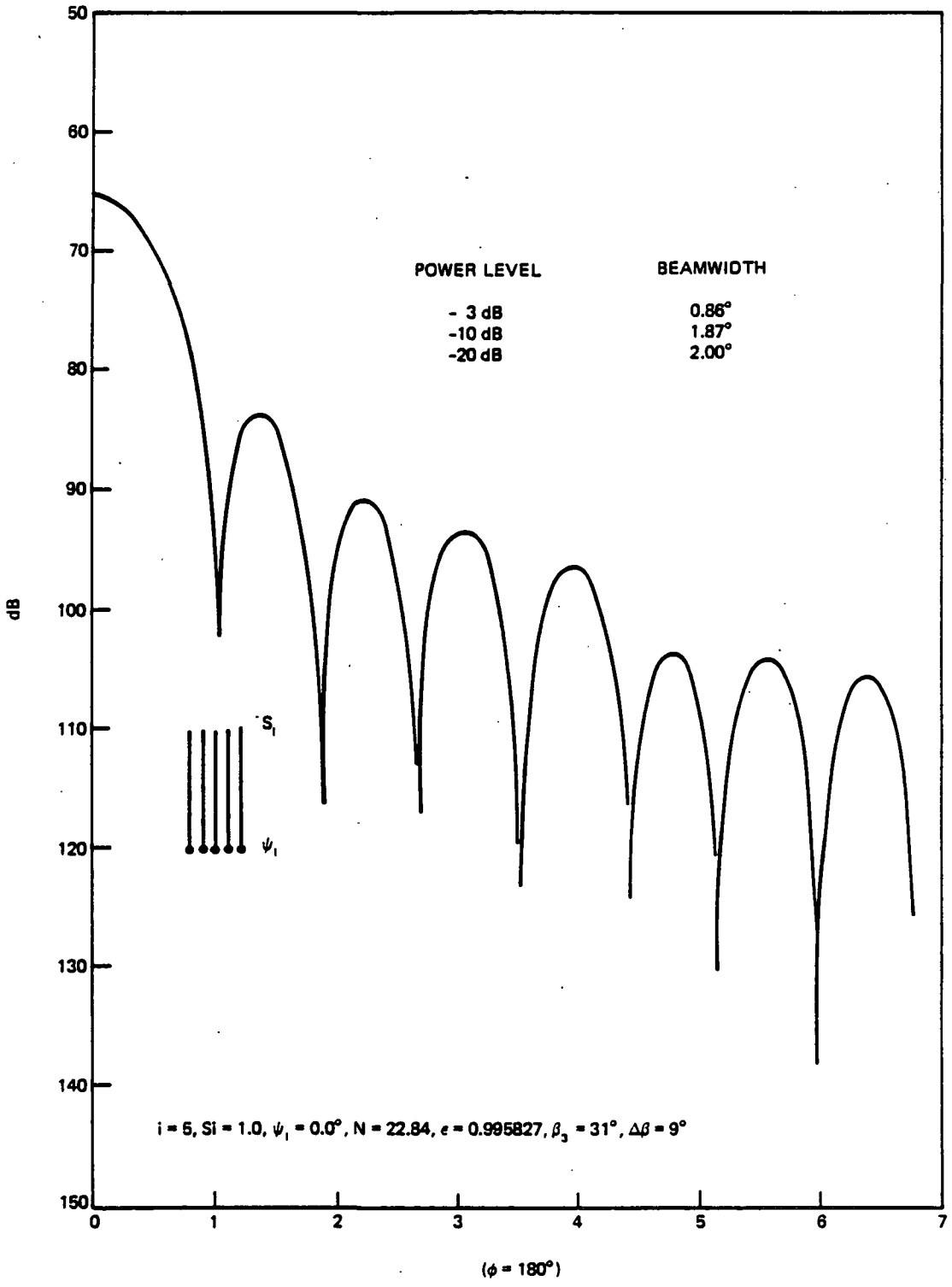

Figure 16. Secondary radiation pattern obtained with five-beam primary feed.

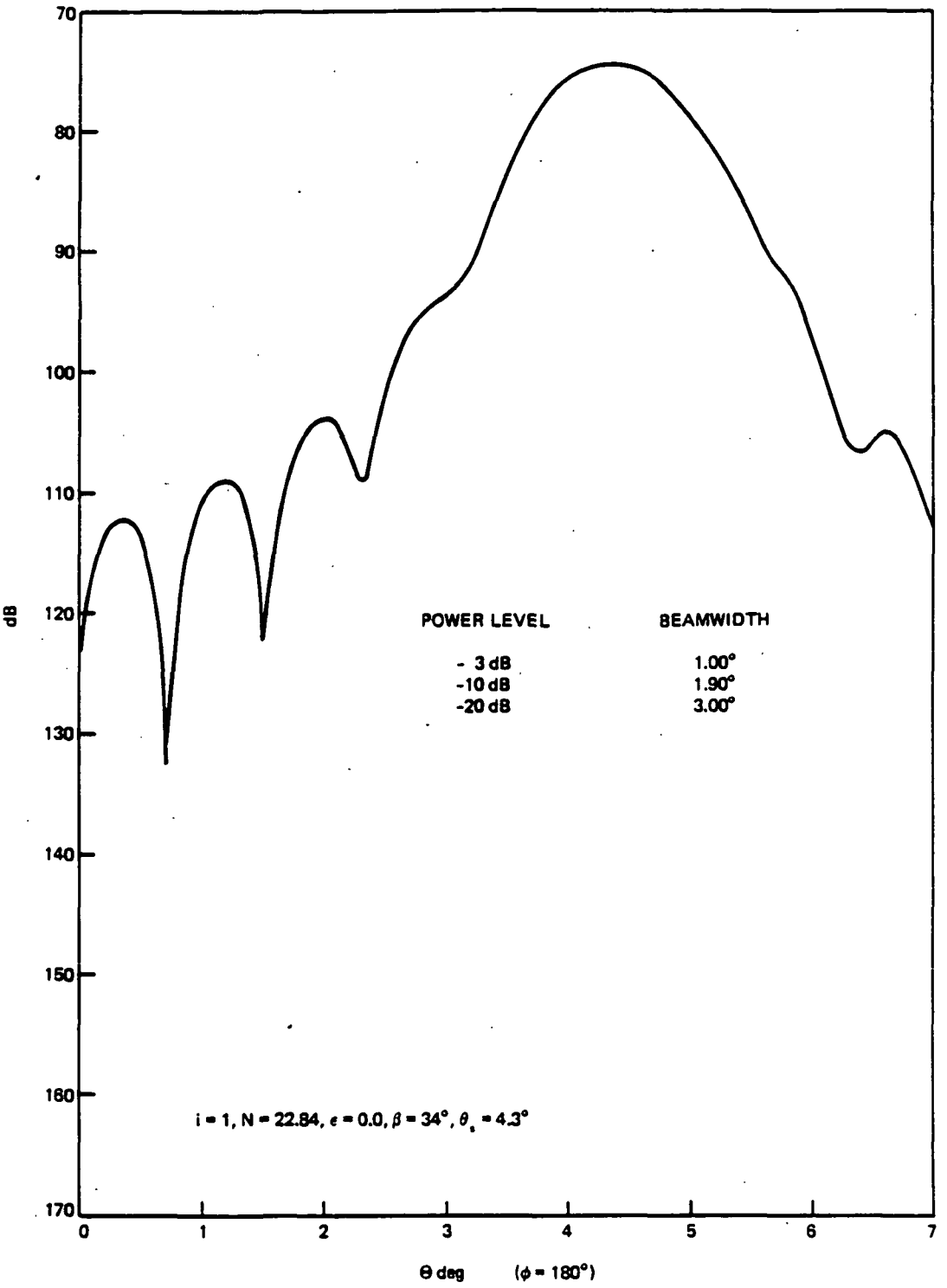

Figure 17. Reference pattern.

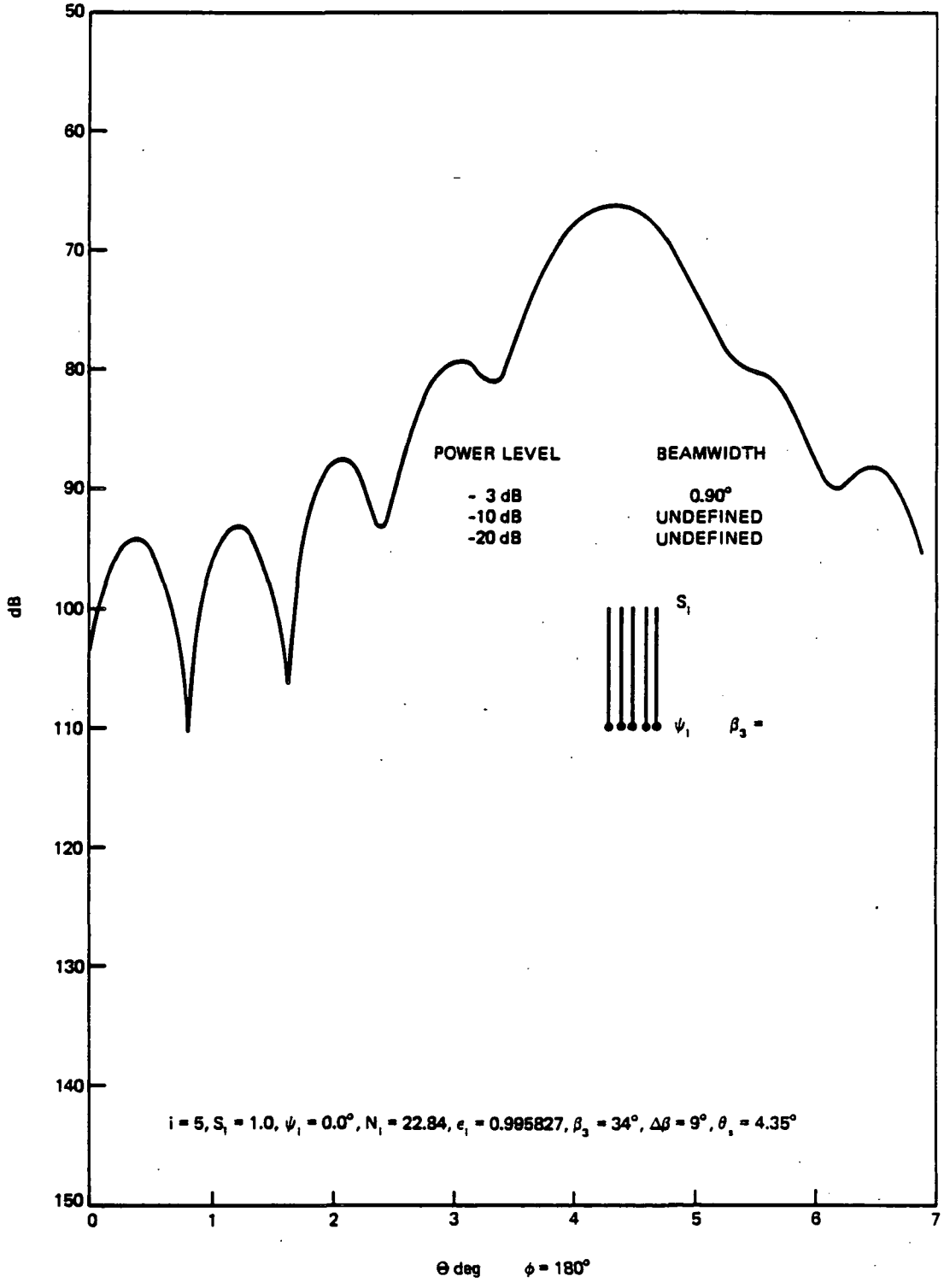

Figure 18. Secondary radiation pattern obtained with five-beam primary feed.

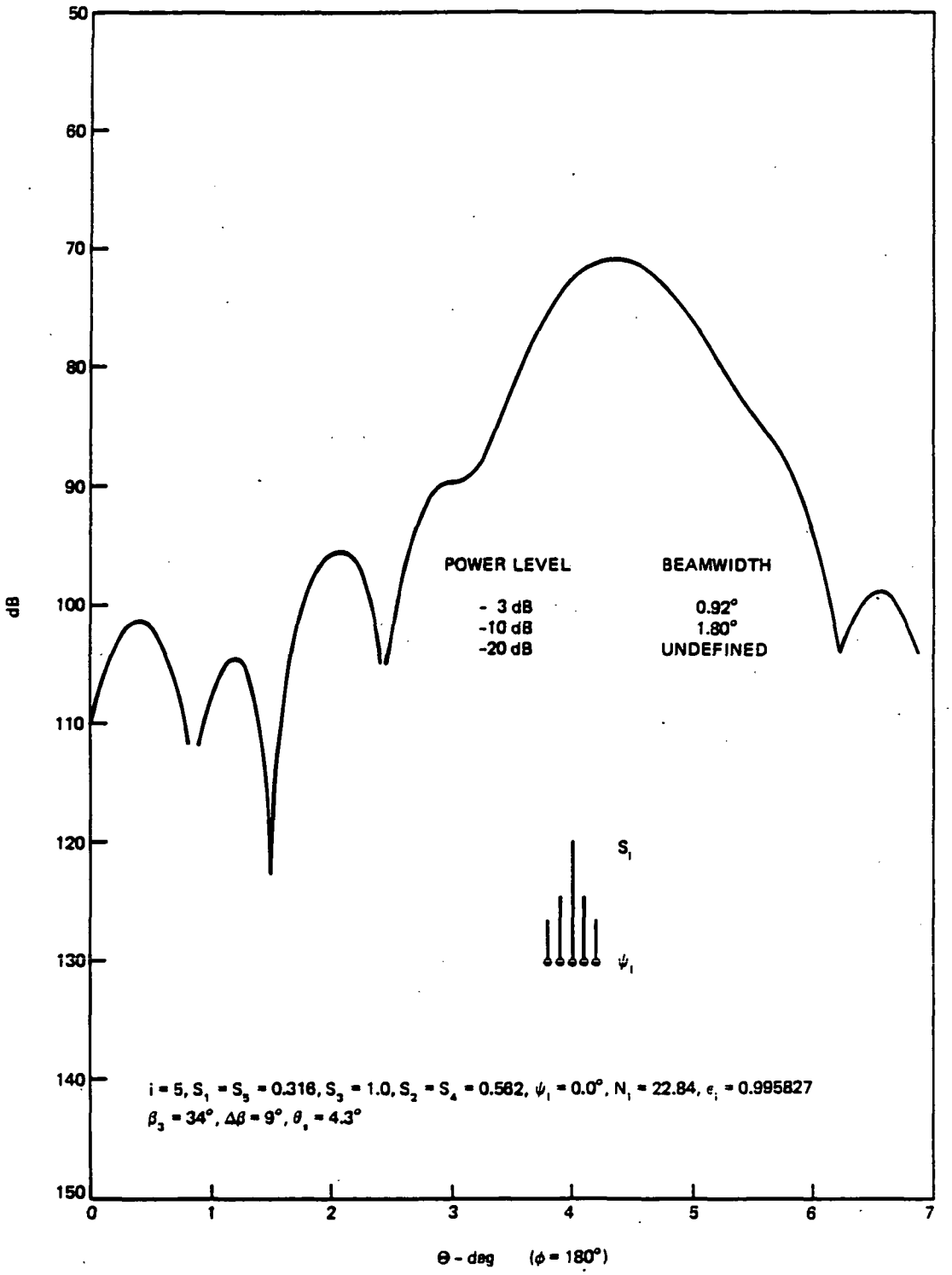

Figure 19. Secondary radiation pattern obtained with amplitude-tapered five-beam primary feed.

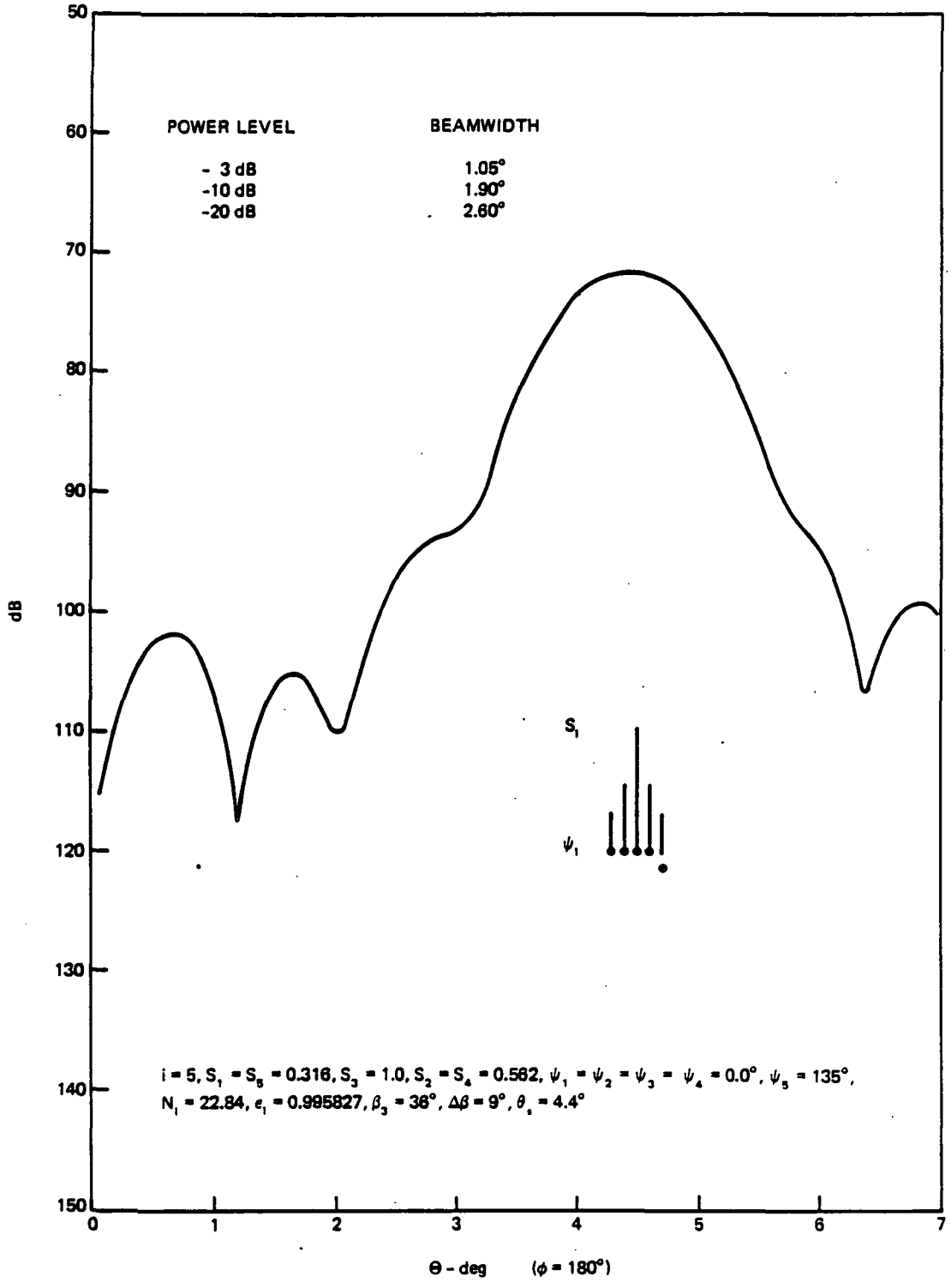

Figure 20. Secondary radiation pattern obtained with phase/amplitude-tapered five-beam primary feed.

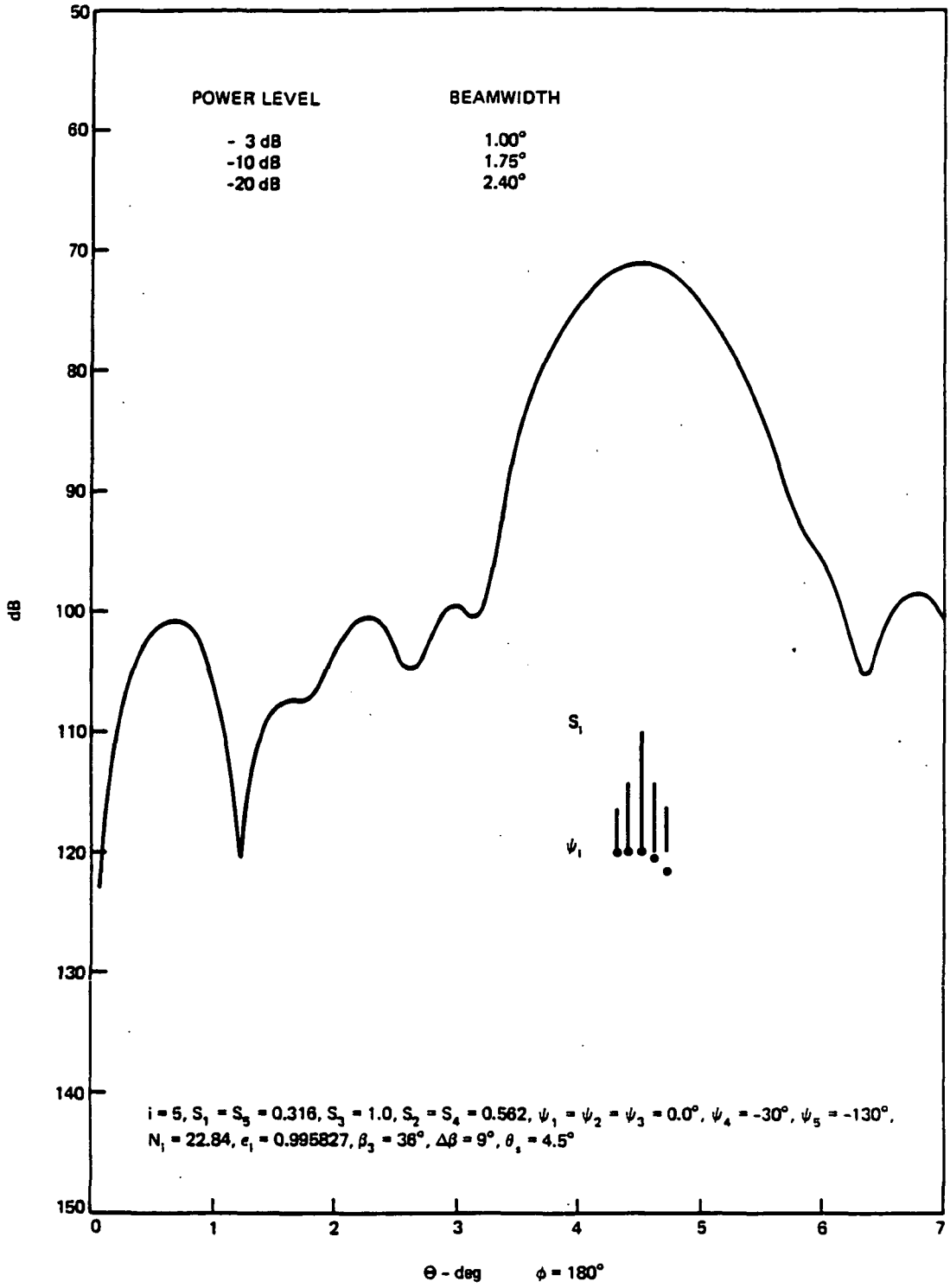

Figure 21. Secondary radiation pattern obtained with phase/amplitude-tapered five-beam primary feed.

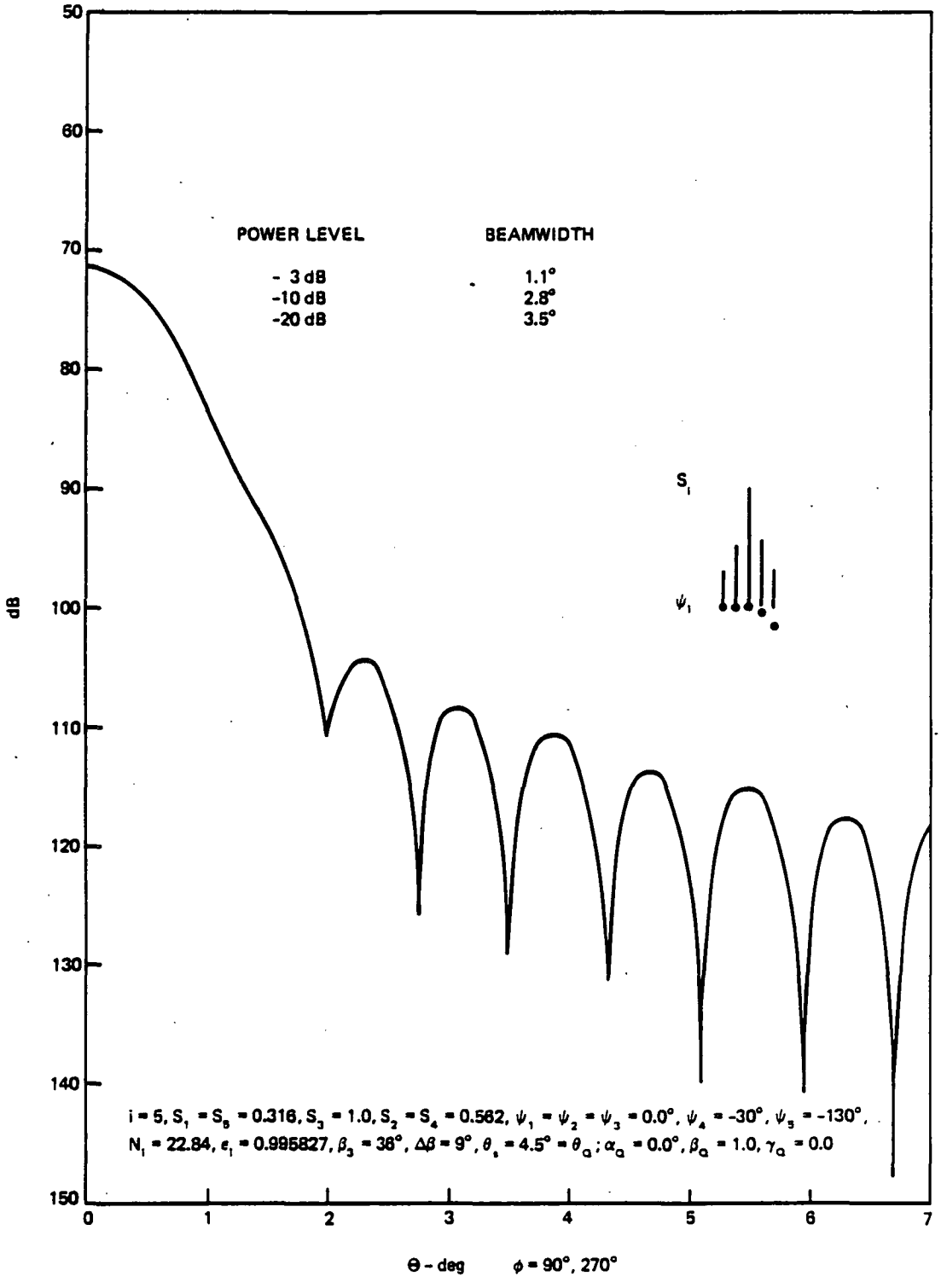

Figure 22. Secondary radiation pattern obtained with phase/amplitude-tapered five-beam primary feed.

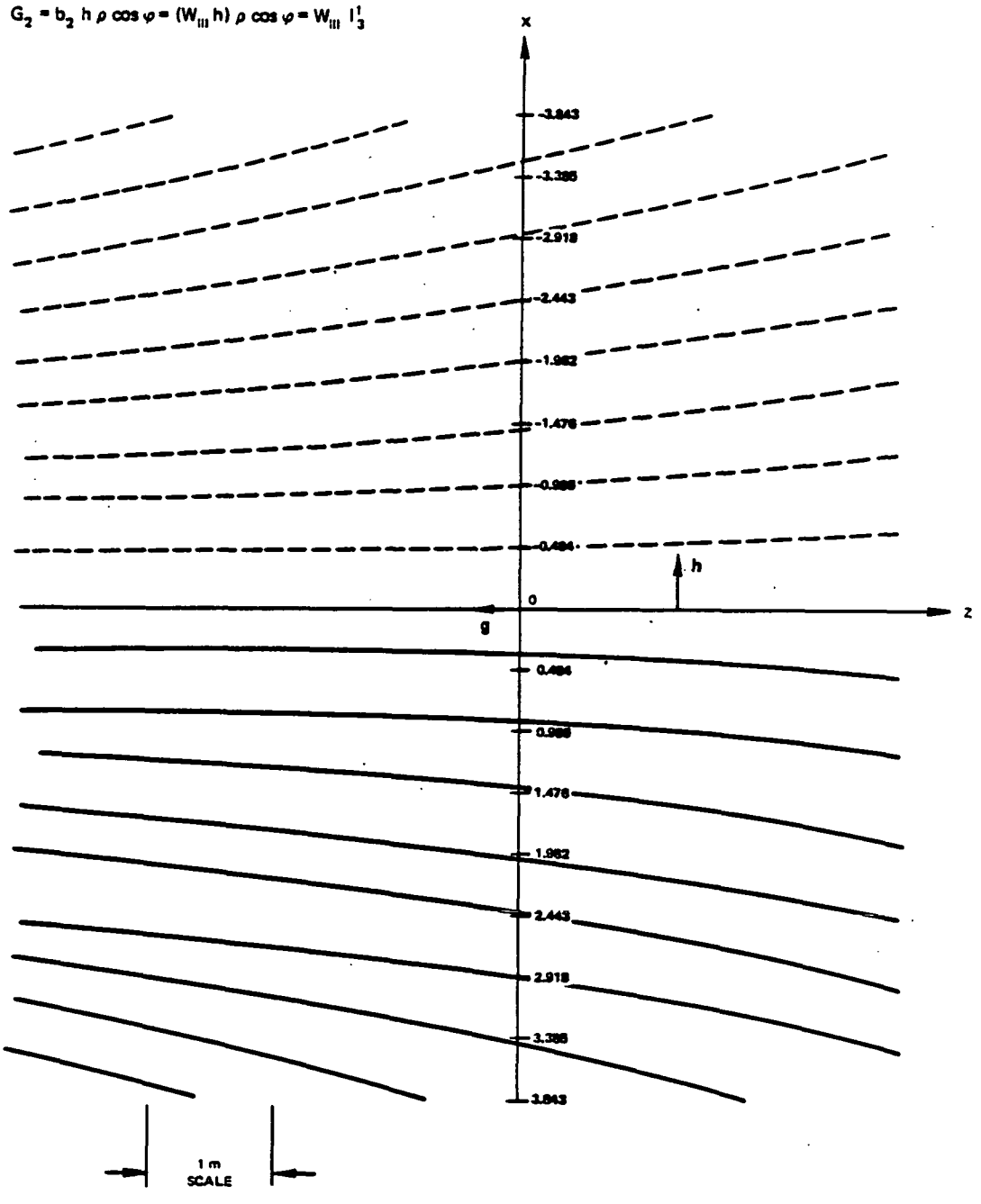

Figure 23. Lateral focus coefficient (W_{111} h) for parent paraboloid.

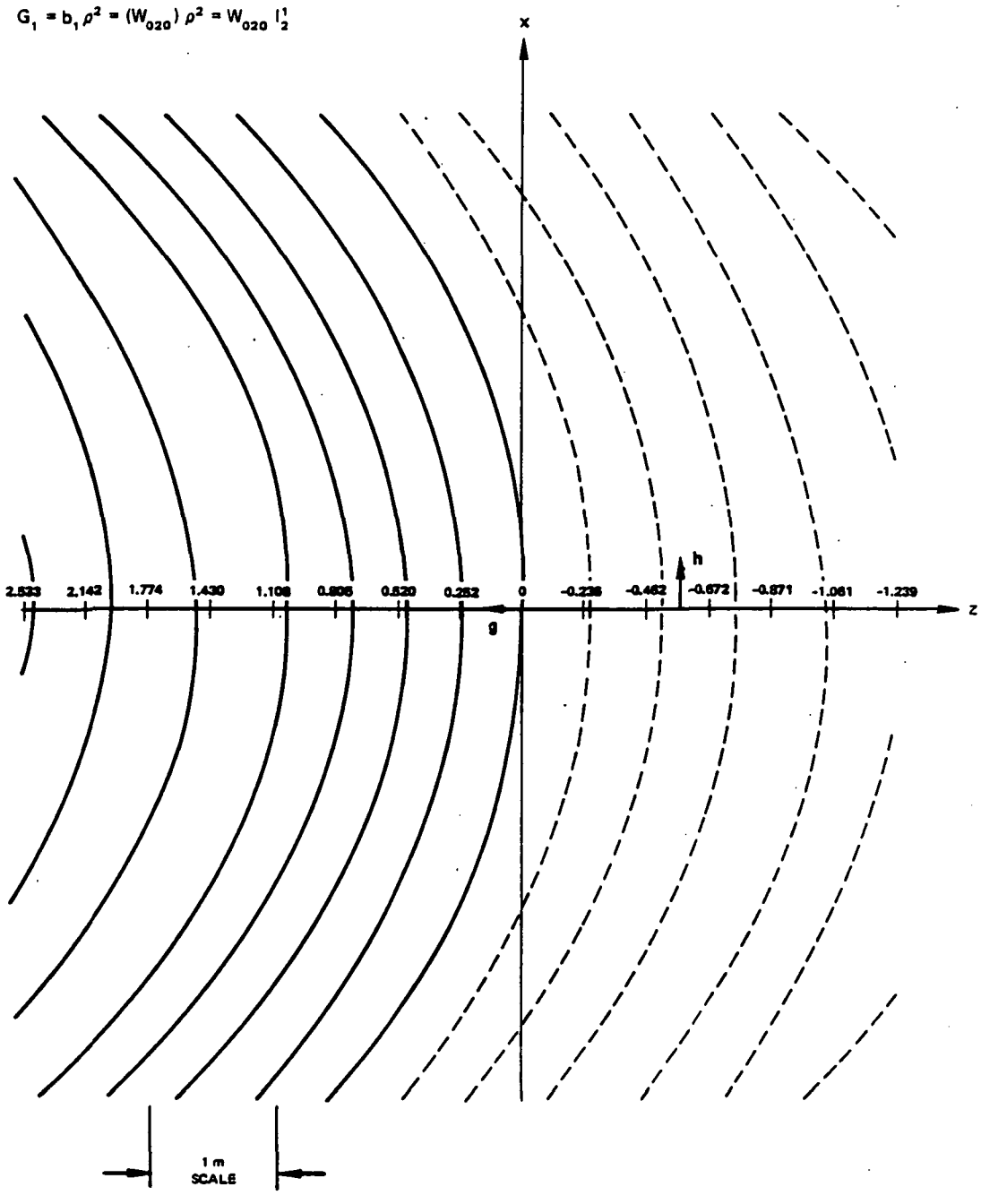

Figure 24. Axial focus coefficient (W_{020}) for parent paraboloid.

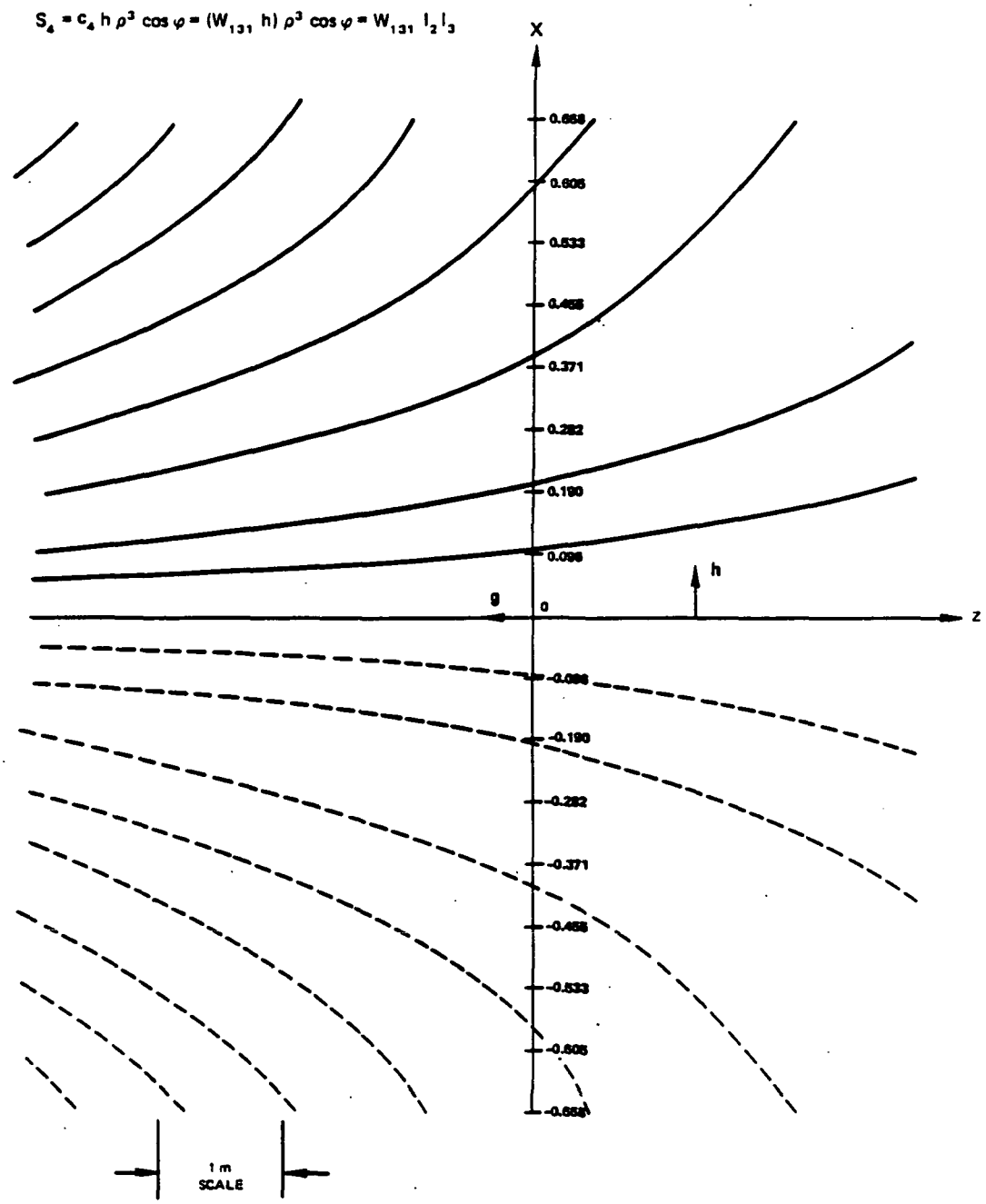

Figure 25. Coma coefficient (W_{131} h) for parent paraboloid).

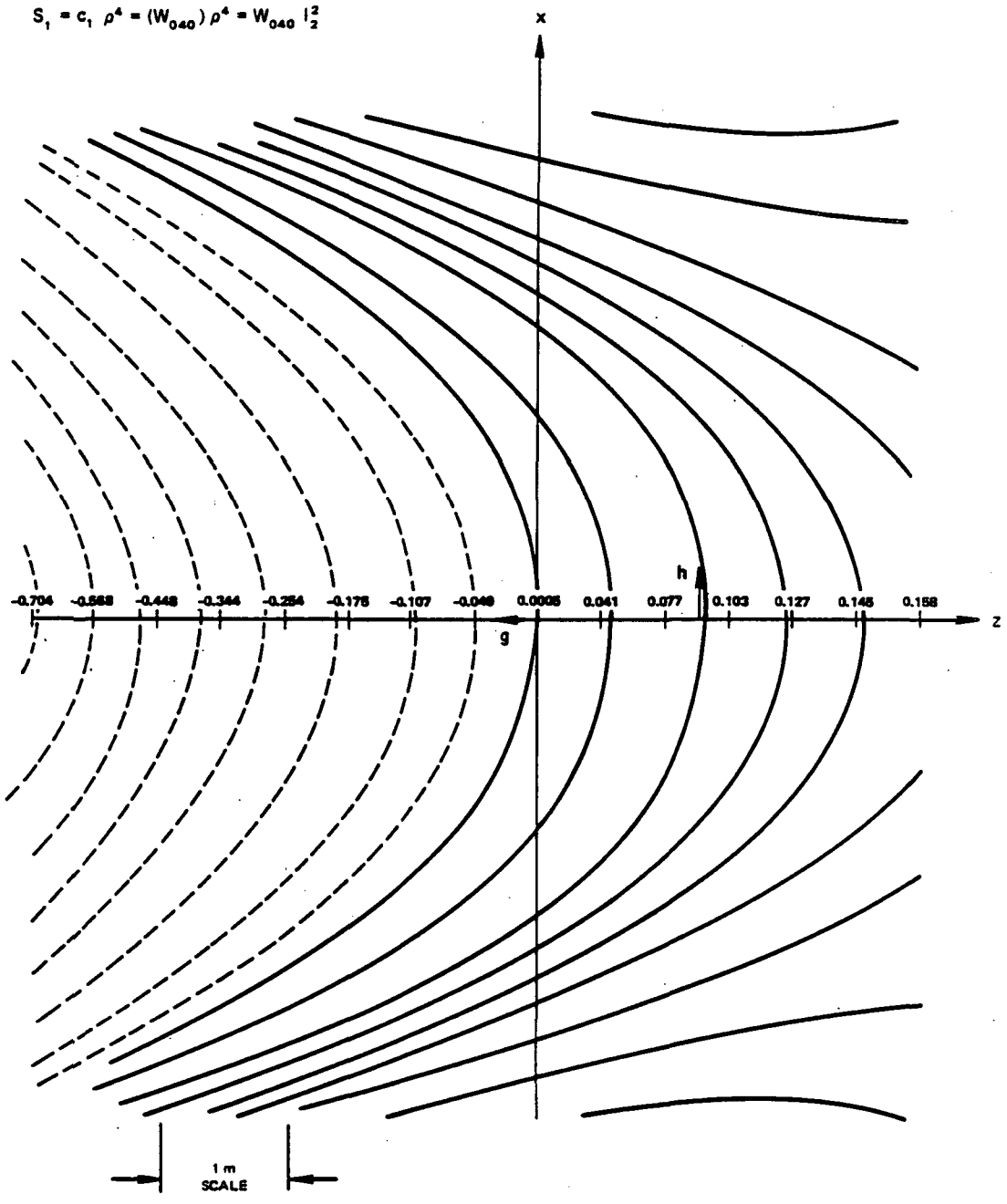

Figure 26. Spherical coefficient (W_{040}) for parent paraboloid.

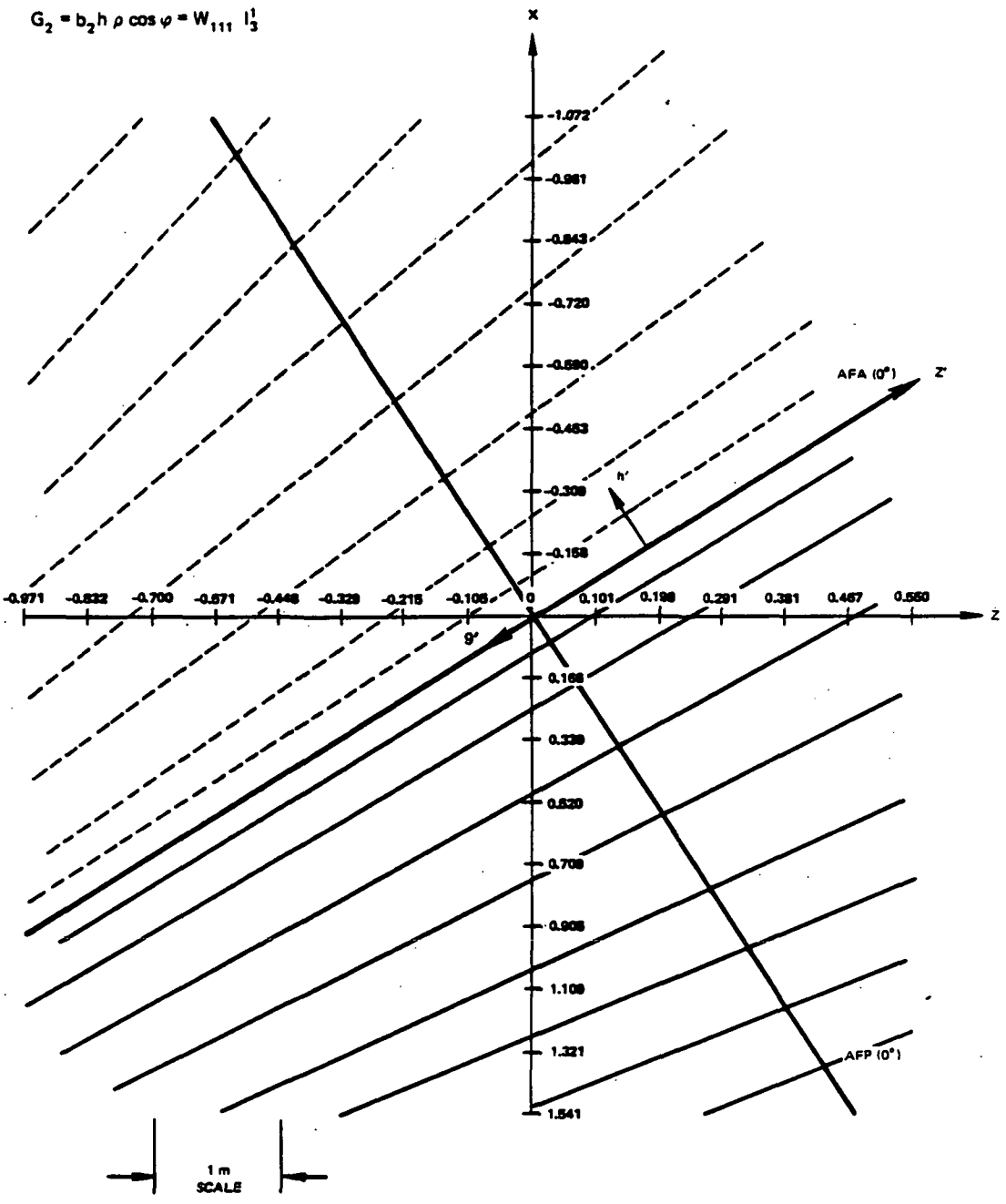

Figure 27. Lateral focus coefficient (W_{111} h) for offset paraboloid.

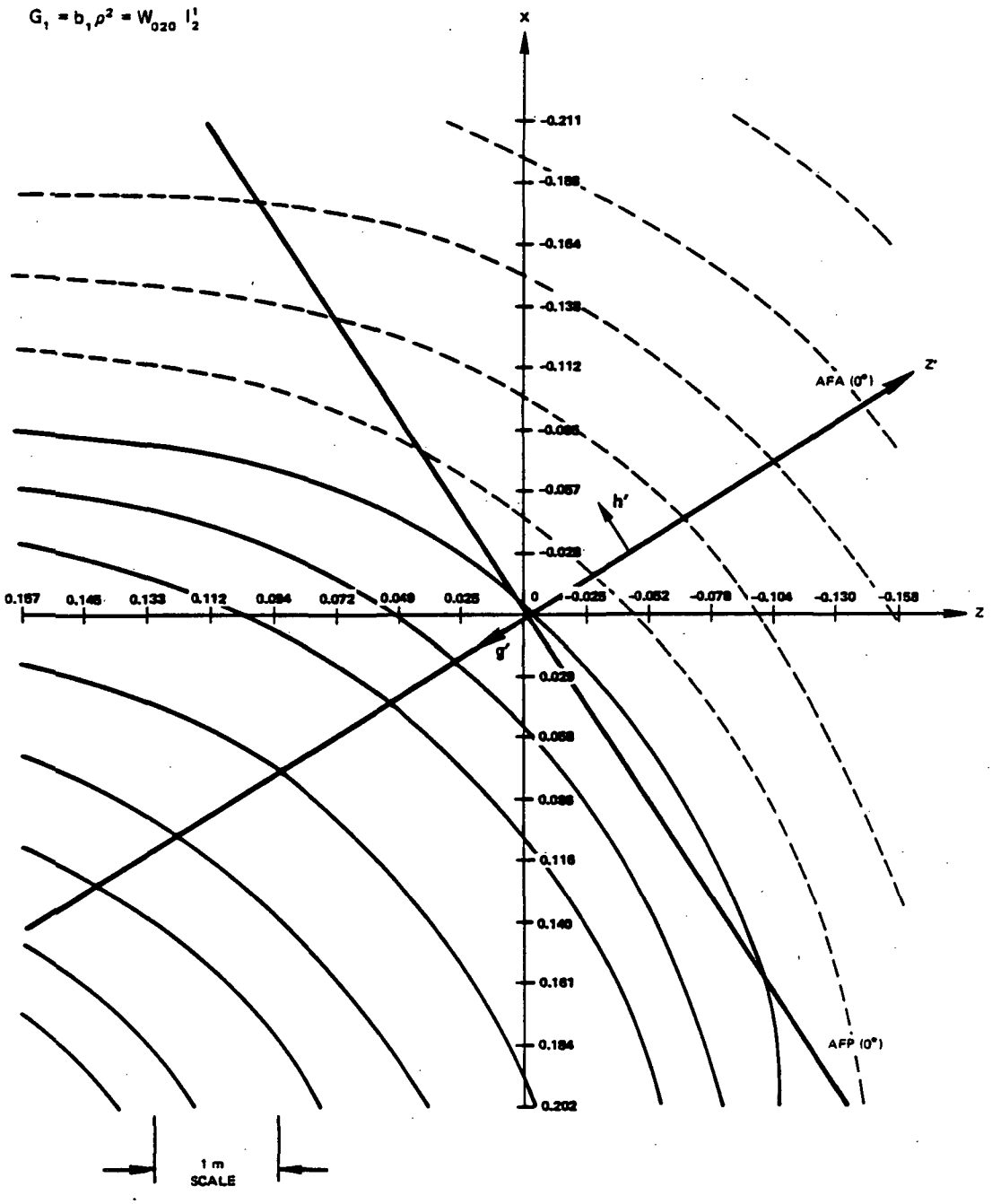

Figure 28. Axial focus coefficient (W_{020}) for offset paraboloid.

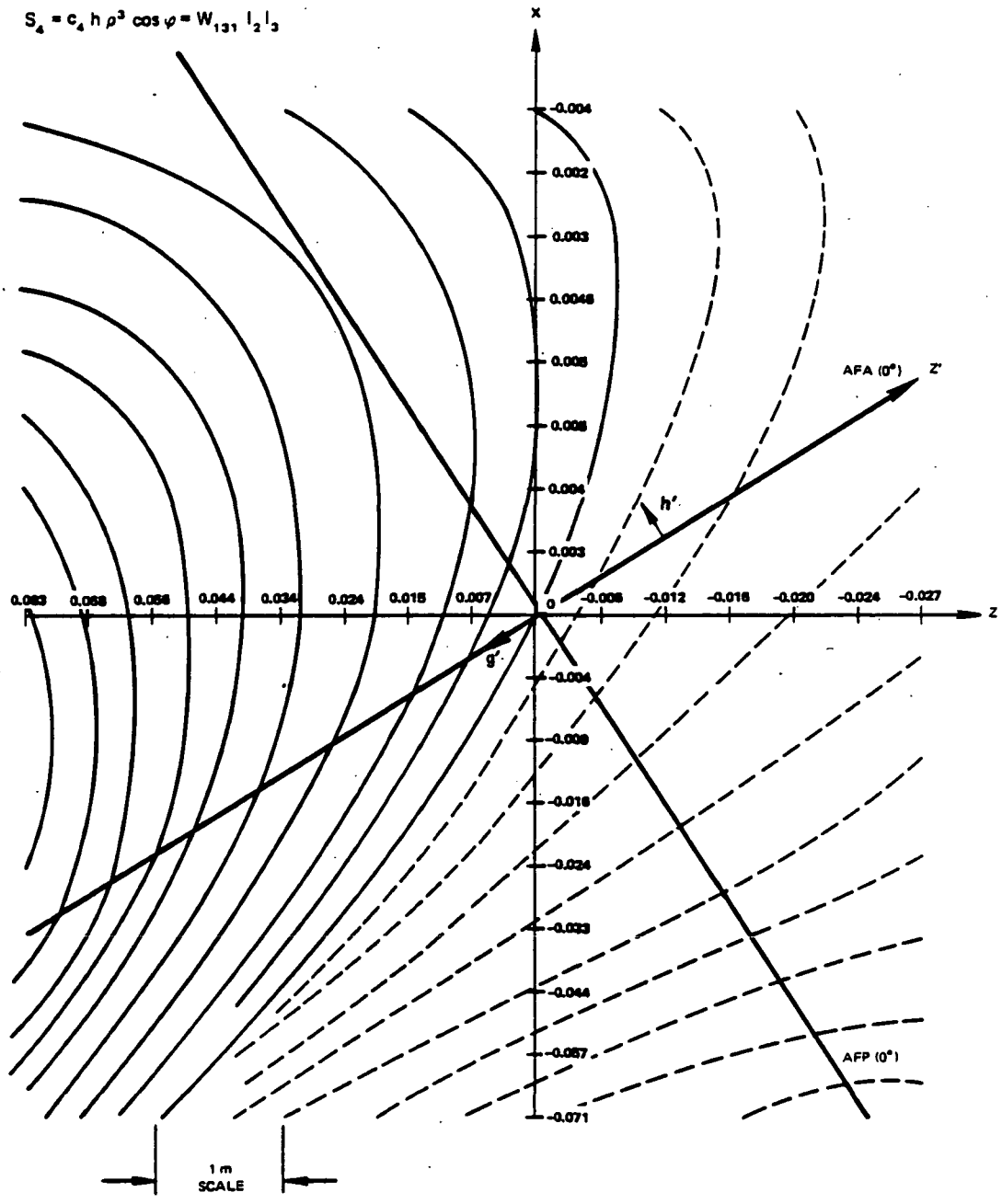

Figure 29. Coma coefficient (W_{131} h) for offset paraboloid.

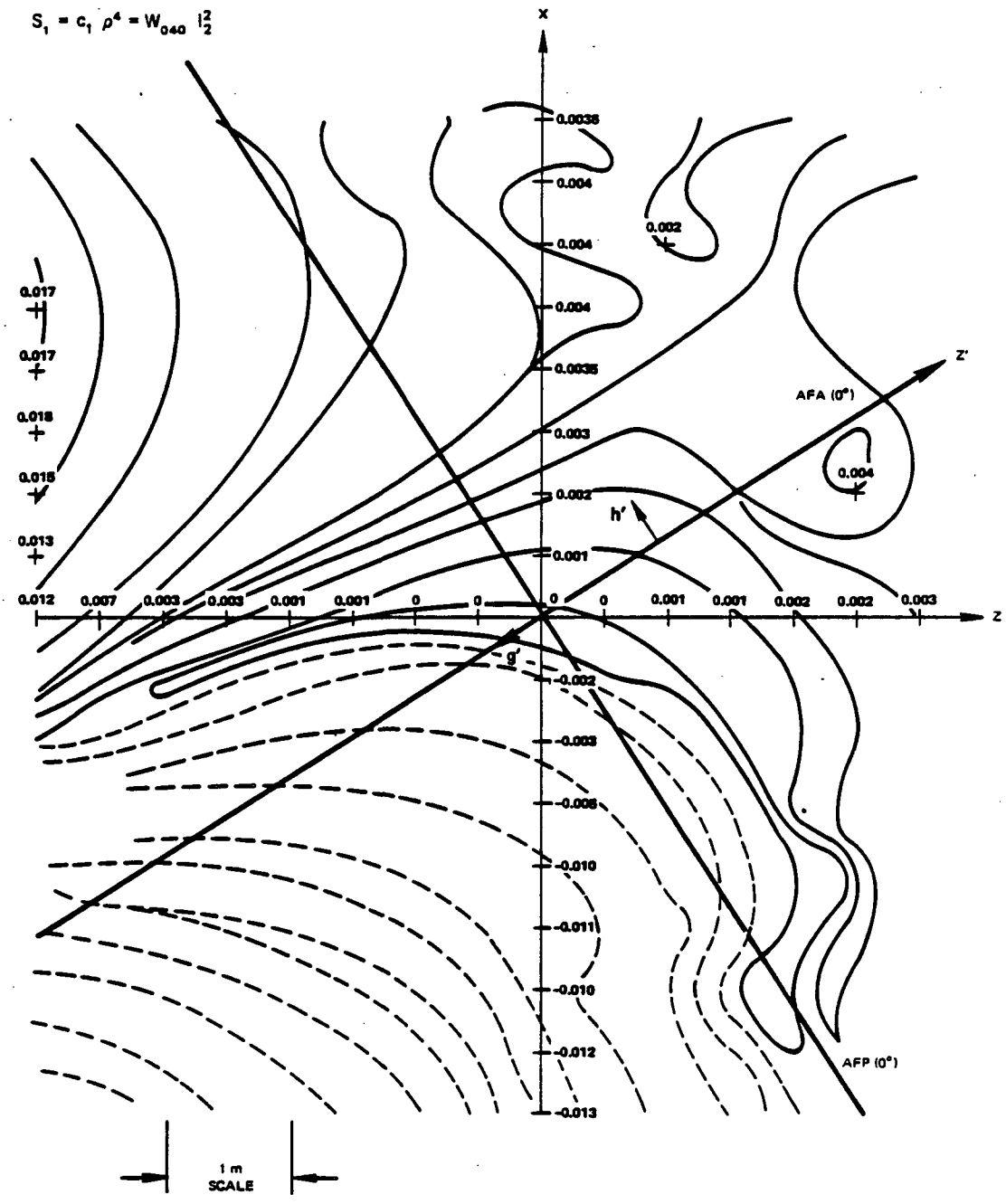

Figure 30. Spherical coefficient (W_{040}) for offset paraboloid.

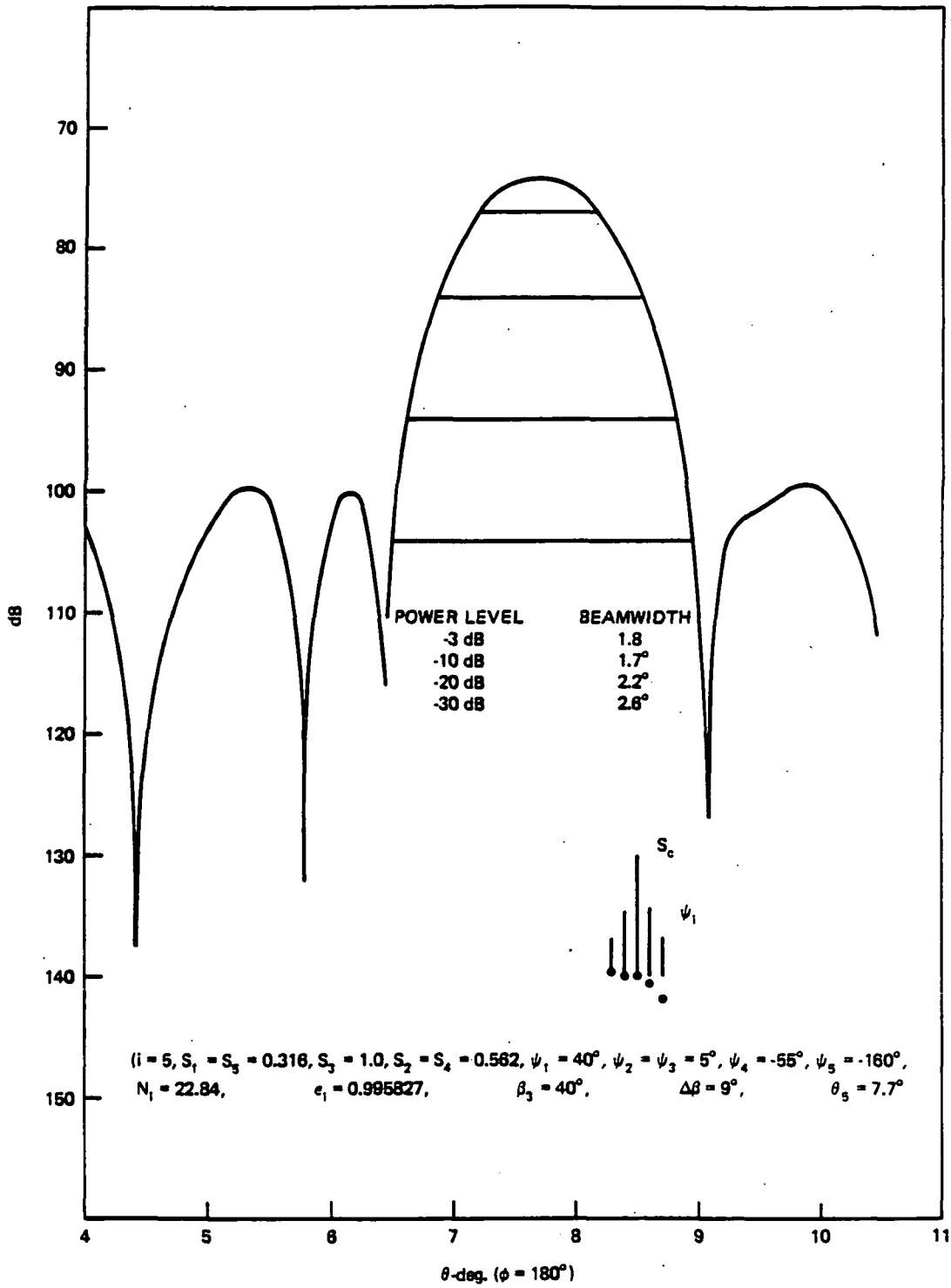

Figure 31. Secondary radiation pattern obtained with phase/amplitude-tapered five-beam primary feed.

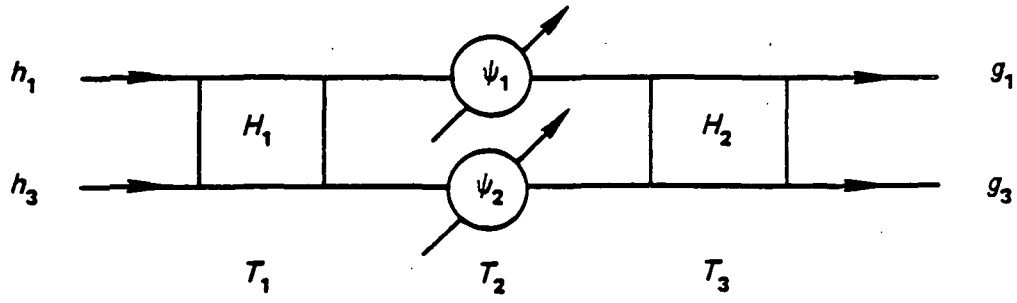

Figure 32. Weighting circuit.

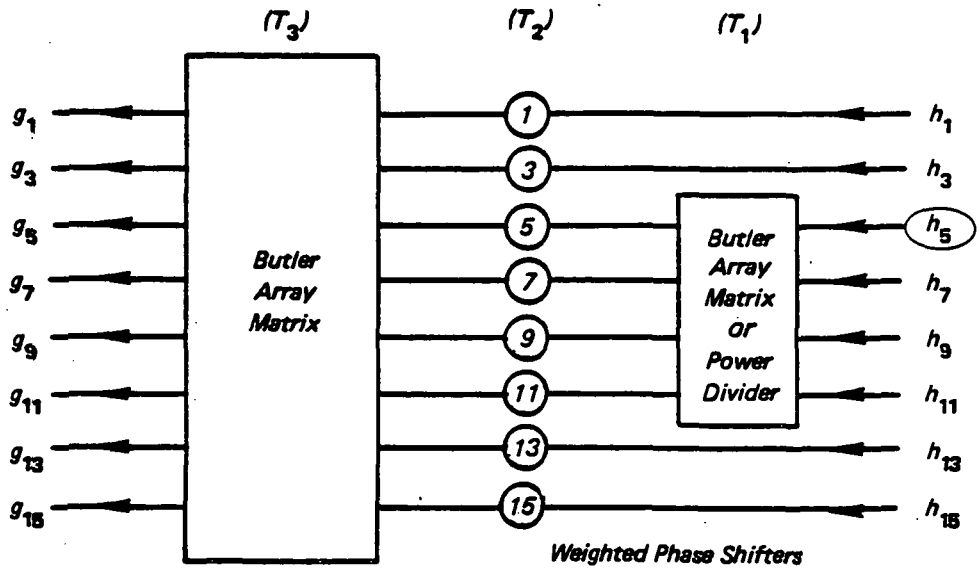

Figure 33. Circuit for coma correction.

APPENDIX A

ABERRATIONS

The optical invariants are:

$$I_1 = h^2, \quad I_2 = \rho^2, \quad I_3 = h\rho\cos\phi \tag{A-1}$$

and the optical path difference is:

$$\text{OPD} = \delta = \sum_{l,m,n} W_{2l+n,2m+n,n}\, h^{2l+n}\rho^{2m+n}\cos^n\phi \tag{A-2}$$

Let the Cartesian aperture coordinates be

$$x = \rho\cos\phi, \quad y = \rho\sin\phi \tag{A-3}$$

Then the classical "aberrations" of Gauss, Seidel, and Schwarzschild of mixed degree (2), (4), (6) are easily generated in terms of the optical invariants as follows. The aberration name is sometimes redundant in the literature.*

*W. L. Wolfe, "The Infrared Handbook," Environmental Research Institute of Michigan, Library of Congress Cat. Card No. 77-90786, 1978; and E. H. Linfoot, *Recent Advances in Optics*, Oxford, 1955.

DEGREE (0)	–		
–	$H_o = a_o$	=	W_{000}

DEGREE (2)	GAUSS		
–	$G_o = b_0\, h^2$	=	$W_{200}\, I_1^1$
Axial Focus	$G_1 = b_1\, \rho^2$	=	$W_{020}\, I_2^1$
Transverse Focus	$G_2 = b_2\, h\rho \cos\phi$	=	$W_{111}\, I_3^1$

DEGREE (4)	SEIDEL		
–	$S_0 = c_0\, h^4$	=	$W_{400}\, I_1^2$
Spherical	$S_1 = c_1\, \rho^4$	=	$W_{040}\, I_2^2$
Astigmatism	$S_2 = c_2\, h^2\, \rho^2 \cos^2\phi$	=	$W_{222}\, I_3^2$
Field Curvature/Petzval	$S_3 = c_3\, h^2\, \rho^2$	=	$W_{220}\, I_1\, I_2$
Coma	$S_4 = c_4\, h\rho^3 \cos\phi$	=	$W_{131}\, I_2\, I_3$
Distortion	$S_5 = c_5\, h^3\, \rho \cos\phi$	=	$W_{311}\, I_3\, I_1$

DEGREE (6)	SCHWARZSCHILD		
–	$D_0 = d_0\, h^6$	=	$W_{600}\, I_1^3$
Spherical	$D_1 = d_1\, \rho^6$	=	$W_{060}\, I_2^3$
Elliptical Coma	$D_2 = d_2\, h^3\, \rho^3 \cos^3\phi$	=	$W_{333}\, I_3^2$
Elliptical Coma	$D_3 = d_3\, h^3\, \rho^3 \cos\phi$	=	$W_{331}\, I_1\, I_2\, I_3$
Oblique Spherical	$D_4 = d_4\, h^2\, \rho^4$	=	$W_{240}\, I_1\, I_2^2$
Astigmatism	$D_5 = d_5\, h^4\, \rho^2 \cos^2\phi$	=	$W_{422}\, I_1\, I_3^2$
Petzval	$D_6 = d_6\, h^4\, \rho^2$	=	$W_{420}\, I_2\, I_1^2$
Oblique Spherical	$D_7 = d_7\, h^2\, \rho^4 \cos^2\phi$	=	$W_{242}\, I_2\, I_3^2$
Distortion	$D_8 = d_8\, h^5\, \rho \cos\phi$	=	$W_{511}\, I_3\, I_1^2$
Linear Coma	$D_9 = d_9\, h\, \rho^5 \cos\phi$	=	$W_{151}\, I_3\, I_2^2$

IR Handbook: $W_{21+n,\,o,o} \doteq 0$.

APPENDIX B

PHYSICAL OPTICS SIMULATION (RECEPTION)

$$\bar{E}(x,y,z) = \frac{1}{j\omega\epsilon}\,\frac{1}{4\pi}\iint_{\gamma i}\left[(\bar{n}\times\bar{H}_1)\cdot\nabla\right]\nabla\psi\,ds - j\omega\mu\,\frac{1}{4\pi}\iint_{\gamma i}(\bar{n}\times\bar{H}_1)\,\psi\,ds \qquad \text{(B-1)}$$

$$\bar{H}(x,y,z) = -\frac{1}{4\pi}\iint_{\gamma i}(\bar{n}\times\bar{H}_1)\times\nabla\psi\,ds \qquad \text{(B-2)}$$

$$\psi = e^{-jkr} \qquad \text{(B-3)}$$

$$\nabla\psi = -\left(jk + \frac{1}{r}\right)\psi\,l_r \qquad \text{(B-4)}$$

Parameters:

Frequency: f = 1.414 GHz
Diameter of reflector: D_0 = 15.0 m ⇒ σ_{lmax} = 7.5 m
Central blockage: σ_{lo} = 0.0 m
Reflector displacement: (x_{1p}, y_{1p}, z_{1p}) = (-10.5 m, 0.0 m, -18.0 m)
Focal length: F = 18.0 m
Source function amplitude, phase, polarization: $(S_1, \psi_1, P_1\ (I))$ = (1.0, 0.0°, 1.0)
Source directivity factors: (N, ϵ) = (0.0, 0.0)
Source displacement: $(\bar{\rho}\epsilon) = (x_e, y_e, z_e)$ = (-22.689 X 10^3 m, 0.0 m, 148.274 X 10^3 m)
(Range = 150,000 meters)
Source inclination (Euler angles): (α, β, γ) = (90.0°, 0.0°, 351.3°)
Integration sampling interval: (LI) = 1.0 (λ), (Fig. 9)

Source function:

$$\mathcal{F} = \frac{\cos^N\Theta}{\left[\sin^2\Theta\cos^2\Phi + \dfrac{\sin^2\Theta\sin^2\Phi + \cos^2\Theta}{(1-e^2)}\right]^{1/2}} = 1.0 \qquad \text{(B-5)}$$

under N = ϵ = 0.0 for plane-wave simulation (remote spherical source).

1. Report No.	2. Government Accession No.	3. Recipient's Catalog No.
TM-86090		

4. Title and Subtitle	5. Report Date
The Correction of Aberrations Computed in the Aperture Plane of Multifrequency Microwave Radiometer Antennas	May 1984
	6. Performing Organization Code: 913
7. Author(s): R. F. Schmidt	8. Performing Organization Report No.: 84F0267
	10. Work Unit No.: 506-54-26
9. Performing Organization Name and Address: Goddard Space Flight Center, Greenbelt, Maryland 20771	11. Contract or Grant No.
	13. Type of Report and Period Covered: Technical Memorandum
12. Sponsoring Agency Name and Address: National Aeronautics and Space Administration, Washington, D.C. 20546	14. Sponsoring Agency Code

15. Supplementary Notes

16. Abstract

This document develops an analytical/numerical approach to identifying and correcting the aberrations introduced by a general displacement of the feed from the focal point of a single offset-paraboloid antenna used in deployable radiometer systems. A 15-meter reflector with 18-meter focal length is assumed for the analysis, which considers far-field radiation pattern quality, focal-region fields, and aberrations appearing in the aperture plane. The latter are obtained by ray-tracing in the transmit mode and are expressed in terms of optical notation. Attention is given to the physical restraints imposed on corrective elements by real microwave systems and to the intermediate near-field aspects of the problem in three dimensions. The subject of wavefronts and caustics in the receive mode is introduced for comparative purposes. Several specific examples are given for aberration reduction at eight beamwidths of scan at a frequency of 1.414 GHz.

17. Key Words (Suggested by Author(s))	18. Distribution Statement
Radiometers, Diffraction, Coma Correction	STAR Category 33 Unclassified – Unlimited

19. Security Classif. (of this report)	20. Security Classif. (of this page)	21. No. of Pages	22. Price
Unclassified	Unclassified	70	A04

For sale by the National Technical Information Service, Springfield, Virginia 22161